DETECTION AND STUDIES OF RADIO SIGNALS ASSOCIATED WITH UHE COSMIC RAY SHOWERS IN THE ATMOSPHERE.

A Thesis
Submitted to the University of Gauhati as the Fulfilment of the Requirements for the Degree of Doctor of Philosophy in Physics in the Faculty of Science, 2010

By

NAYANMONI SAIKIA
DEPARTMENT OF PHYSICS
GAUHATI UNIVERSITY
GUWAHATI-781014
ASSAM, INDIA

Dr. Kalyanee Baruah
Professor , Department of Physics
&
Dr. P.K. Boruah
Professor
Department of Instrumentation & USIC

GAUHATI UNIVERSITY
Gopinath Bordoloi Nagar
Guwahati-781014
ASSAM, INDIA

CERTIFICATE

This is to certify that Mr. Nayanmoni Saikia, M.Sc. has worked under our guidance and supervision since March 2003 for his thesis entitled "**Detection and Studies of Radio Signals Associated with UHE Cosmic Ray Showers in the Atmosphere**" which is being submitted to the Gauhati University for the award of the Degree of Doctor of Philosophy. This thesis is based on original work done by Mr. Saikia. He has fulfilled all the requirements under the Ph.D. regulation of Gauhati University. He has also published a few original research papers in reputed Conference Proceedings, Journals and few are communicated for publication. He has also presented research papers in the International and National conferences.

Neither the thesis nor any part of it has been submitted to any other University or Institution for any other degree.

29-6-10
(Kalyanee Boruah)

29.6.10
(P.K.Baruah)

DECLARATION

I wish to state that the work embodied in this thesis entitled '**Detection and Studies of Radio Signals Associated with UHE Cosmic Ray Showers in the Atmosphere**" forms my contribution to the research work carried out under the guidance **Prof . Kalyanee Baruah**, Department of Physics, Gauhati University and **Dr. P.K. Boruah,** Department of Instrumentation & USIC, Gauhati University and I am submitting this for the award of the Degree of Doctor of Philosophy in the faculty of Science, Gauhati University. I here by declare that neither the thesis nor any part of it had been submitted to any other University or Institution for any other degree.

Date: 29/06/2016
Place: Guwahati

Nayanmoni Saikia
(Nayanmoni Saikia)

# ACKNOWLEDEMENT

First of all I would like to thank my esteemed research supervisors Prof. Kalyanee Boruah, Department of Physics, Gauhati University and Prof.P.K.Boruah, Department of USIC & Instrumentation, Gauhati University for their valuable guidance and meticulous supervision in my every stage of present research work. Prof. Kanlynee Boruah and Prof. P.K.Boruah has been taking active interest in my work and has also been giving right advice to me from the start of my Ph.D work. I am very grateful for their patience, motivation, enthusiasm and immense knowledge in the field of Cosmic Ray research. My words will never be adequate to express my gratitude towards them..

I express a deep sense of gratefulness to Dr. Jyoti Prasad Phukan, Assistant Professor, Department of Physics, DSHK College, Dibrugarah for his selfless endeavour to introduced me first with Prof. P.K. Boruah and Prof. Kalyanee Boruah.

I also acknowledge Dr.Uamananda Goswami, Assistant Professor, Department of Physics, Dibruagarah University for his invaluable suggestions during my research work.

I would also like to specially acknowledge to Mr. Simanta Hazarika for his endless help during my research work.

I would like to acknowledge ISRO, Bangalore, Government of India for funding the research project.

I also express my deep sense of gratitude to Prof. S.K.Gupta, Principal Investigator, GRAPES for giving me the opportunity to visit Cosmic Ray Laboratory (CRL), TIFR, Ooty, and Prof. P.K.Manoharan, NCRA, TIFR, Ooty for his valuable suggestion and guidance during my stay in his institute.

I also like to appreciate Prof. B.S. Acharya, High Energy Group, TIFR, Mumbai for his suggestions and advice relating to our works duringhis visit to our miniarray laboratory, Dept. of Physics, Gauhati University.

I would also like to acknowledge the authorities ofNCRA, TIFR, Pune for arranging the accommodation in NCRA campus during my one week visit in 2005. In this context, I would like to offer my gratitude to Prof. Anand Krishnamurthy, NCRA, TIFR, Pune for his valuable advice and cooperation during my visit to NCRA, TIFR, Pune. I specially thank for his efforts to accompany me to the GMIT site, Pune.

I would also like to acknowledge Dr.Lionel Loudnet, SID monitoring station, France for his continuous guidance on the simulation of Loop Antenna.

I would like to thank Prof. A Rahman, former HOD, Physics Department, GU and the faculty members of Department of Physics, GU Prof.H L Das, Prof. S A S Ahmed, Prof D K Choudury, Prof. B K Sarma, Prof. H L Duorah, Dr K Duorah, Dr B Bhattacharjee, Dr M P Bora, Dr D Sarkar, Ms B Tiru and Dr. Kushal Kalita.

I would like to thank my all friends Mr. Prasant Konch, Mr. Birinchi Chutia, Mr. Ajoy Sarmah, Mr. Durbajyoti Buragohain, Mr. Nitul Saikia, Mr Hemanta Dutta, Mr. Suren Dutta, Mr. Ulen Konuwar and my cousin brother Mr. Mintu Saikia. I also express my thanks to Mr. Hiranya Saikia, Mr. Jadabendra Saikia and Mr. Khirod Saikia for their support in my research work.

I also take the opportunity to express my thanks toDr. T Bezboruah, Reader, Department of Electronics and Telecommunication, Gauhati University, the pioneered of miniarray lab and my co-workers Dr. Subash Chand Rajbongshi,Mr. Hamen Medhi, Mrs. Dipsikha Kalita, and Mr. Chabin Thakuria.

I also acknowledge Dr. Mrinal Kumar Das, Dr. Ranjan Sarma, Mr. Kumud Bora, Ms. Barnali Debnath, Miss Rupjyoti Gogoi, Miss Hizam Zeen Devi, Mr. Ambeswar Gogoi and all the boarders of V. V. Rao research scholars hostel.

At this moment I would like to express my deep honour and unreturnalble indebtedness to my father Sri Ghana Saikia, my mother Srimati Ambika Saikia who's nursing with an unlimited care grown up me to this position. My younger brother Sri Sankar Jyoti Saikia, younger sisters Mrs Banalata Saikia, Mrs Jahnabi Saikia, my elder sister Kabita Saikia, Sister-in-law Mrs Kabita Gogoi, Brother-in–law Mr. Mridul Bora, Mr. Jagadish Borua and Mr. Prasanta Handique, are very much kind to me and provide me with their moral supports and cooperation to continue my research wok. I, therefore take the opportunity to convey my gratefulness to all of them.

I also acknowledge with gratitude to my father in law, mother in law, my sisters in law and brother in law for their support and help during my Ph.D work.

At this very moment I express my deep love and affection to my two years old son Mr. Bedanta Saikia. His every activity is the source of inspiration for me to do my research work.

In addition to this all individuals, I must thank with love to my wife Mrs. Markynti Swer without whose constant encouragement, support and co-operation, I could not have completed this thesis work in time.

ABSTRACT

The study of Ultra high energy cosmic rays (UHECRsenergy 10^{17}eV) has gained much importance due to astrophysical aspects related toGreisen- Zatsepin-Kuzmin (GZK) cut-off and primary mass composition. Different experimental projects are going on to detect UHECRs, by measuring different measurable parameteis of Extensive Air Shower (EAS) produced by primary particle of UHECRs in the atmosphere. Among these measurable parameters, radio signal associated with UHECRs isone, which was detected for the first time by J.V Jelley of UK and his co-workers in 1965. In 1970ties the measurement of these radio pulses became unreliable mostly due toradio interference, and other methods like direct ground based particle detection or fluorescence measurement gained importance. Today, due to the advent of new technology as well as high speed digital data processing techniques renewed efforts have been made to make radio method for the detection of UHECRs a powerful and effective ɓol that compliments the established techniques very well.

The measurement of radio pulses from air shower has a number of advantages: It gives much higher duty cycle than measuring optical light, and it is complementary to the detection of the particles that reach the ground level. Moreover, it is unaffected by attenuation, gives calorimetric measurement of an air shower and provides high directional accuracy.

Charge excess mechanism proposed by Askarayan and Geomagnetic charge separation mechanisms produce HF (>1MHz) radio waves due to UHECRs. The production mechanism of the LF & VLF (<1MHz) radio signal due to UHECRs is explained on the basis of the electromagnetic phenomenon of transition radiation.

The main aim of this work is to investigate the properties of radio signal from the UHECRs with the help of existing GU miniarray particle detectors and radio antennas.
The present work consists of the following parts-

i) Renovation of miniarray

At the very beginning we tested and calibrated miniarray particle detectors. A trigger circuit has been designed and implemented using CPLD (Complex Programming Logic Device) for the miniarray particle detectors. This unit is tested and simulated using VHDL (Very high speed Integrated Circuit Hardware Description Language). The trigger circuit selects UHECRs from the pulse trains produced by the miniarray particle detectors.

ii) Theoretical model of Loop antenna

To receive the LF/VLF radio signal we used circular loop antenna. The working and characteristics of small circular loop antenna has been simulated using LTspiceIV. AC analysis of the loop antenna has been done for four different load resistances. Noise analysis has been done for three different atmospheric noise levels with minimum and maximum noise expected values being defined by ITU-R P.372-8. Finally SNR of the loop antenna has been computed.

iii) Experimental setup for radio signal reception

For the detection of radio signal in the LF/VLF region two loop antennas are used. Signals from the antenna are processed by the VLF/LF front end electronics before transmitting to the control room for recording. The front end electronics of the VLF/Lf radio detection consists of one low noise preamplifier and a band pass filter. Two such VLF/LF pulse receiving radio systems were fabricated based on the simulation results on LTspice. This is tested and calibrated with the standard field method before installing in the rooftop of Physics building near the miniarray hut. To ensure the coincidence between the two radio channels, one channel is used to trigger the other channel.

Received Signal is recorded through DSO (TDS 500A- Tektronix) and stored in PC via GPIB (NI 488 ™) interface. Power spectral density of the receiving signal was calculated and thereby using the calibration factor the induced magnetic field and finally induced electric field is computed. Attempt is made to explain the results on the basis of transition radiation model.

iv) Radio Channel in coincidence with miniarray

To detect the coincidence between particle pulses and radio signals, miniarray and radio detecting channel were run simultaneously. However, no coincidence was observed while miniarray pulse was used as trigger to record the radio signals.

v) Transition Radiation Model

A model has been developed to calculate the field strength of the radio signal from UHECRs in VLF/LF region on the basis of transition radiation mechanism. It is found that this mechanism of radio emission may be very effective if the antennas are located outside the shower disk.

CONTENTS

LIST OF FIGURES

CHAPTER I

Introduction

The study of cosmic rays is one of the most active fields in astroparticle physics research. Their origin, acceleration, and transport to earth have been some of the unsolved problems in the astrophysics for nearly 100years. To resolve these questions, a large detector which combined multiple detection techniques with higher duty cycles, are needed. We have investigated an alternative way to study cosmic rays: measuring the radio emission from cosmic ray air shower. It is unaffected by attenuation, has a high duty cycle promising to help solving the mystery of cosmic rays.

Radio pulses from cosmic ray air showers were first discovered by Jelley et al. in 1965 at 44MHz [Jelley65]. The results were soon verified and in the late 1960's emission from 2MHz up to 520MHz were found. In the following years these activities ceased almost completely mostly due to difficulties with radio interference, uncertainty about the interpretation of the results and success of other methods.

Measuring the radio pulses from air shower has a number of advantages. If one can deal with radio frequency interference (RFI) it allows for round clock measurements, giving a much higher duty cycle than e.g. measuring fluorescence light. The signal is integrated over the whole air shower evolution, making it complementary to measuring the particles that reach the ground level. And because radio pulse is not quantized like the particle signal one can get better direction estimate for the air shower.

In the high frequency domain Geo-Synchrotron and Charge Separation are the responsible mechanisms for the radio emission from air shower. But in the low frequency (LF) as well as very low frequency (VLF) these two mechanisms fail to predict any observable radio emission from cosmic ray air shower. Only possible radio emission in the

LF/VLF region can be due to transition radiation mechanism. When the excess electrons of an EAS incident on the earth surface, due to the sudden change of the dielectric in the path of these electrons, transition radiation phenomenon occurs and LF/VLF radio emission take place.

After giving an introduction of cosmic rays, air shower and relevant experiment, I present the instrumentation and data acquisition method that were developed as part of this thesis, and discuss the results of the radio signal detection.

1.1 Cosmic Rays

The earth is continuously bombarded by highly energetic rays coming from outside the earth's atmosphere. This cosmic radiation was discovered by Victor Hess in 1912 during balloon experiments. He found that the intensity of ionizing radiation above 1000m height rises with increasing height and accounted this to radiation from outside the earth atmosphere [Hess12]. Cosmic rays primarily consist of atomic nuclei with masses ranging from protons (hydrogen) to Uranium. Electrons and gamma–quanta make up less than 1% of the flux. The energy range of cosmic rays spans from some MeV to more than 10^{20}eV. The arrival directions of the cosmic rays are distributed uniformly over the sky, only little anisotropy has been found at the highest energies.
Up to now there is no universally accepted theory for the origin of the primary particles at high energies, their acceleration, or their reactions in the interstellar medium during their transport to earth. Finding the sources of cosmic rays and understanding the mechanism that accelerates them to such a high energies is one of the unsolved mysteries of astronomy.

When a cosmic ray particle hits a nucleus of an atom of the earth atmosphere it undergoes a nuclear reaction and produce several secondary particles. These secondary particles can again react with atmospheric nuclei and produce more secondary particles. Together these secondary particles form an extensive air shower.

Cosmic rays are also of concern for the public. The secondary particles of air showers form a significant fraction of the natural radioactivity on earth. Neutrons in air showers produce the radioactive ^{14}C isotope that is used for archaeological age determination. It has been also proposed that cosmic rays affect the weather and thus can play a role in climate change [Shaviv05]. So the study of cosmic rays, their arrival directions, energy spectrum, and chemical composition is of interest for a number of branches of physics.

1.1.1 Energy Spectrum

Over a wide range of energy the primary cosmic ray flux follows a simple power law

$$\frac{dN}{dE} \propto E^{-\gamma} \qquad (1.1)$$

At 10^{11}eV about one particle per second per square meter hits the earth, these changes to approximately one particle per year per square meter at 5 $\times 10^{15}$eV, and above 10^{19}eVonly about one particle per century and per square kilometer hits the earth.

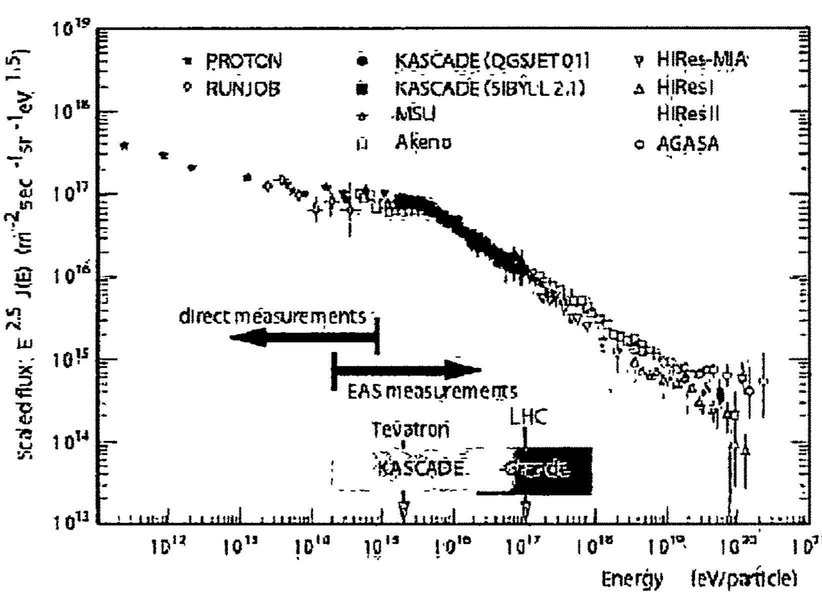

Figure 1.1 Spectrum of the cosmic ray flux, taken from [Haungs04]. The flux has been multiplied by a factor of $E^{2.5}$. This emphasizes the so called knee at $\sim 5\times 10^{15}$eV and ankle at 5×10^{18}eV in the spectrum.

In the first approximation the power law index γ in equation (1.1) is equal to 2.7. In detailed view of the figure 1.1 we see that γ is not constant but changes slightly- the two most important regions of changes are named- knee at energy 5×10^{15}ev and ankle at energy 2×10^{19}eV. At the knee position the spectrum become steeper, changes the value of power law index γ, going from $\gamma \approx 2.7$ to $\gamma \approx 3.1$. The probable cause for the knee is different acceleration mechanisms for energies below and above the knee. Effects during the transport through the interstellar medium and the fact that Protons can't be confined by galactic magnetic field, causes decrease in flux.

At the highest energies above 10^{18}eV as shown in figure 1.1 the spectrum becomes flatter. This ankle could be caused by the transition from galactic to extragalactic components. Sharp decrease in flux at 5×10^{19}eV is predicted by Greisen- Zatsepin-Kutz'min effect [Greisen66][Zatsepin66]. This describes that high energy proton above $\sim 5\times10^{19}$eV loose energy by producing pions in reactions with photons of the cosmic microwave background.

At energies below 10^{10}eV the flux and direction of cosmic rays is affected by the solar wind and the magnetic field of earth and sun. This part of the spectrum shows the 11-year variability in flux and is clearly associated with solar activity. At higher energies these affect can be neglected.

Observations of primary cosmic rays are carried above the Earth atmosphere and orbital probes, rockets and high-altitude balloons are used for the detection. Due to the very low flux, these techniques can't be applied to detect primary cosmic rays beyond 10^{15}eV. On the other hand measurements of cosmic ray induced air showers are possible starting at this energy range.

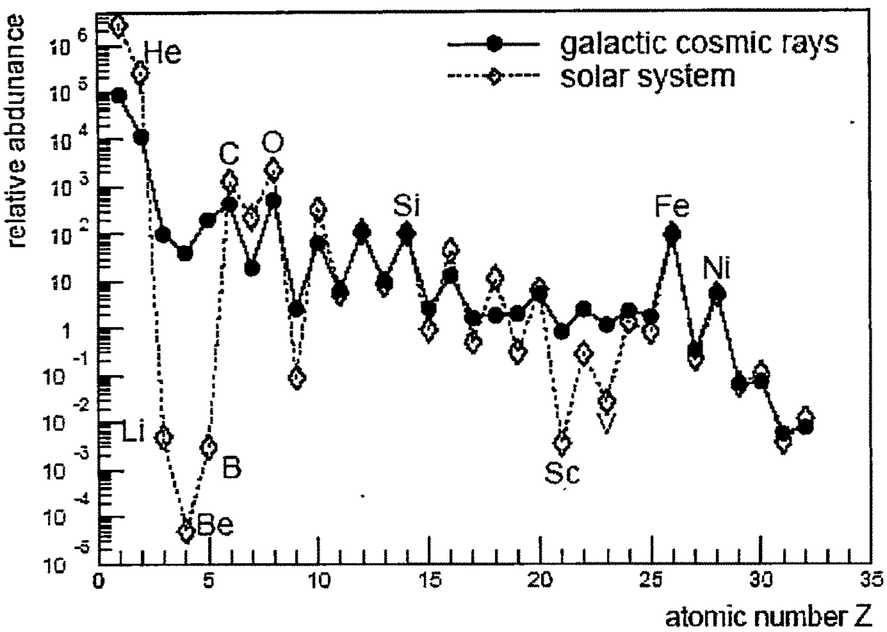

Figure 1.2 Chemical composition of the cosmic radiation with less than 2GeV/nucleon compared to the composition in the Solar System. Normalized to Si=100[Wefel91]

1.1.2 Chemical Composition

With direct measurement it is possible to make a detail analysis of the chemical composition of the cosmic radiation. Figure 1.2 shows the relative abundance of the different chemical elements for cosmic rays with less than 2GeV/nucleon compared to the composition in the solar system.

The composition of cosmic ray within this energy range and that of solar system agree to a large extent. This signifies to a common origin of the matter in the solar system and the matter in the cosmic radiation. Two discrepancies remain:

1. The light elements hydrogen and helium are less common in the cosmic radiation, than in the solar system. This is probably due to the high ionization energy of these elements that suppress the initial acceleration of those elements [Horneffer06]

2. Lithium, beryllium, and boron as well as the elements from scandium to manganese are more common in the cosmic radiation. These elements are produced during the transport of the cosmic rays by spallation of nuclei from C(C, Si, Ge, Sn& Pb), N (N,P,As,Sb & Bi),O(O, S, Se,Te & Po) or the iron (Fe, Ru & Os) group.

At higher energies the chemical composition can only be deduced by comparing the results of air shower measurements to the results of simulations of air showers. As air showers have high statistical fluctuations and simulations have large uncertainty, the indirect determination has larger errors than the direct measurements.

At the highest energies the chemical composition is still largely unknown. It is due to the fact that determination of chemical composition is based on interpreting the air shower data with nuclear interaction model, which is to be extrapolated from low energy data. Thus it is still unclear whether highest energy cosmic rays are mainly protons or heavy nuclei [Watson06].

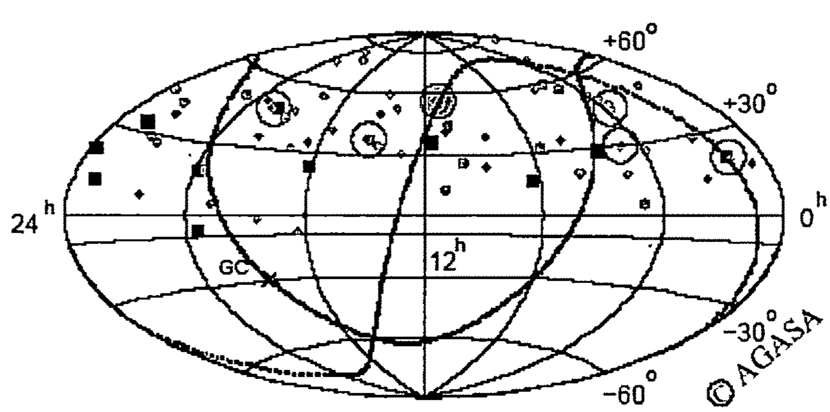

Figure 1.3 Arrival directions of cosmic rays with energies above 4×10^{19}eV as measured by AGASA experiment. Green circles represent events with E > 4×10^{19}eV, and red squares those with E>10^{20}eV. Shaded circles indicate event clustering within the angular resolution of 2.5^0 [Takeda 99].

1.1.3 Anisotropy

The location or concentration of the arrival direction distribution of cosmic rays in a particular region of celestial sphere is defined by the term anisotropy. The cosmic rays are deflected by the Galactic magnetic fields which confine the particles in the Galaxy and homogenize their arrival directions. The spatial distribution of cosmic rays is almost isotropic. Only in the low energy region an excess is observed in the direction of the sun. Many analyses were done in the lower energy regions and summarized in [Watson92].

Some signs of slight anisotropy were observed in the energy region, where the Larmor radius is growing above the kilo-parsec order, above 10^{17}eV. In the data from Havarah Park was found the amplitude with an excess of about 2% at the right ascension $212^0 \pm 17^0$ in the energy region about 10^{17}eV. 1.4 % excess at the very different right ascension 123^0 in the energy region 3×10^{16}-3×10^{17} eV in Yakutsk data. Other interesting sign of anisotropy was found in the AGASA data between 8×10^{17}-2×10^{18} eV (4.3×10^4 events), where the first harmonic amplitude of 4 % was found in the direction to the Galactic centre [Prouza01].

Stereo data collected by HiRes experiment over a six year period are examined for large scale anisotropy related to the inhomogeneous distribution of matter in the nearby universe. They found that HiRes data with threshold energies of 40 EeV and 57 EeV are incompatible with the matter tracer model at a 95% confidence level unless $\theta_s > 10°$, where, θ_s is the typical deflection angle and are compatible with an isotropic flux. The data set above 10 EeV is compatible with both the matter tracer model and an isotropic flux [Abbasi10].

The analysis of the distribution of the arrival directions of the highest energy event collected by the Pierre Auger Observatory provided an evidence of anisotropy of UHECRs [PAC07]. In this work, it has been shown that there is a significant excess of cosmic rays with energy above 5.7×10^{19}eV within $\sim 3.2^0$ of the position of AGN of Veron-Cetty catalogue located at a distance smaller than 75Mpc from the earth [PAC07[[Ryu09].

1.1.4 Origin, Acceleration and Propagation

The origin, acceleration mechanism and propagation of cosmic rays above 10^{14} eV could not been properly addressed till date. The great energy range and the features in the energy spectrum suggest that different kind of sources is responsible for the cosmic radiation at different energies. In the energy range between 10^{9}eV up to near the knee region cosmic rays are of Galactic origin [Bhattacharjee00] and possibly emitted from supernovae remnant. Below the energy ~ 10^{9}eV the intensity of cosmic rays is temporally correlated with the solar activities, which confirms the solar origin at this energy level [Bhattacharjee00]. The possible sources of UHECRs can be addressed as follows.

The conventional scenario of theories of origin of UHECR is the so called bottom up acceleration [Bhattacharjee00], where charged particles are accelerated from lower energies to the highest energies in certain special astrophysical environments.
The main difficulty in this bottom up scenario is that, distance of most favourable sources above 10^{20}eV such as powerful radio galaxies are located at large distances(>>100Mpc), beyond GZK cutoff distance. In an attempt to overcome these difficulties a different model known as top down model scenario has been postulated, where UHECR particles are the decay products of some supermassive X particles of mass >>10^{20}eV.

1.1.4.1 Bottom up Model

In the bottom–up models the acceleration is due to electromagnetic forces. This can be a direct acceleration that requires strong electromagnetic fields or a stochastic acceleration. The primary model for stochastic acceleration is the first order Fermi acceleration [Fermi49]. In this model a charged particle is scattered by magnetic fields and repeatedly traverses a shock front in the interstellar medium. On average it gains energy of $\frac{\Delta E}{E} \propto \beta$ (with β = v/c the speed of the shock front) at each crossing. The second order Fermi-acceleration is less effective. In this model a charged particle is scattered repeatedly at statistically distributed magnetic clouds and gains on average $\frac{\Delta E}{E} \propto \beta^2$ in every cycle.

The charged particles of the cosmic radiation are deflected by magnetic fields in the Milky Way. This confines cosmic rays with energies < 10^{18} eV to the Milky Way and its halo. From the relative abundances of radioactive isotopes one can infer the elapsed time since nucleosynthesis or spallation. With this, the average age of the cosmic rays is estimated to ~ 10^7 years. From the relative abundances of the spallation products one can estimate the traversed matter density of the cosmic rays to ~5 g/cm^2. This entails that the cosmic rays stay mostly in the halo outside of the galactic disc.

Origin in the vicinity of neutron stars in our Galaxy

The nearest suitable UHECR sources should be represented by neutron stars. This source type is not consistent with the assumption of extragalactic origin of UHECRs and has to explain the observed isotropic distribution and no confinement with Galactic plane.
According to the "Hillas plot" [Hillas84] the typical surface strength of magnetic field on young neutron stars is sufficient (~10^{13}G) for the acceleration up to EHECR scale (10^{20}eV for protons). However, the plasma that expands beyond the light cylinder is free from the main loss processes and may be accelerated to ultra-high energies. In particular, newly formed, rapidly rotating neutron stars may accelerate iron nuclei to ultra-high energies through relativistic magneto-hydrodynamic (MHD) winds [Blasi00]. These Galactic sources need enough efficient magnetic fields to isotropize the directions of UHECRs, because no observable correlation with Galactic plane was found.

Origin in radio galaxy hot spots

The hot spots are interpreted as a gigantic shock waves emanating from a central active galactic nucleus at relativistic speeds. Typical size of the hot spot is about few kilo-parsec and the magnetic field within is several hundred μG. The maximum energy attainable is (1-10) $\times 10^{20}$eV, dependent on actual parameters of the spot. The acceleration is classically due to first order Fermi acceleration.

Origin in nearby galaxies

It is generally agreed that our Galaxy is producing cosmic rays up to 10^{18} eV, with luminosity 10^{30} J.s^{-1} for a confinement time 10^{11}s. It is possible that in more active galaxies [Takahara96], with higher rate of star formation, the magnetic field may be higher. The requirement for 10^{20}eV protons exceeds 3×10^{15}G.m (magnetic field $\times$ characteristic size). Acceleration to extremely high energies near the horizons of supermassive black holes in the galactic centers has also been suggested [Boldt99].

Origin in gamma ray bursts

According to some theories [Waxman95] origin of Gamma Ray Bursts (GRBs) may also be a source of ultra-high energy cosmic rays. Both phenomena have still unknown origins and also other similarities that may argue for a common source. UHECRs and GRBs are distributed isotropically, the average rate of γ-ray energy emitted by GRBs is comparable to the energy generation rate of UHECRs of energy $> 10^{19}$eV in a red shift independent cosmological distribution of sources, both have energy $\sim 10^{37}$ J.Mpc^{-3}.yr^{-1}.
The general problem of all the processes described upto this point is that the generated particles have significant energy losses in the vicinity of all these discussed active environments. May be the most important loss channels are due to synchrotron radiation emissions and pair production in the dense surroundings of these objects.

1.1.4.2 Top down Model

Origin in interactions with neutrinos

The first "top-down" acceleration mechanism is represented by the neutrino--neutrino interactions. According to this scenario, the extreme energetic neutrino ($\sim 10^{22}$eV) accelerated in any cosmologically distant source interacts with background relic neutrino (with temperature about 1.9 K) and produces Z^0 boson. The resonance energy for this interaction is about 4×10^{21}eV. This Z boson decays and produces ~2 nucleons, ~ 20 γ-rays and ~ 50 neutrinos. "Z-bursts" are taking place in the relative vicinity (~ Mpc) to the Earth and we observe the arriving nucleons, which are products of Z decay. Other possibility is that the cross-section of neutrino-nucleon interaction rises rapidly in the investigated energy region and these extreme energy neutrinos from the unknown cosmological sources are interacting directly with nucleons in the Earth's atmosphere [Stecker01].

Decay of relic super heavy particles

According to this theory cold dark matter in the galactic halo is supposed to contain a small admixture of long-lived super heavy particles with mass > 10^{21}eV with a lifetime greater than the age of universe [Berezinsky01]. Such particles have to be created during reheating following the inflation or through the decay of hybrid topological defects. The decay products are nucleons, electrons and photons, which are arriving to the Earth and initiating showers with common properties.

Origin in topological defects

Topological defects as monopoles, cosmic strings, and superconducting strings should be also the sources of UHECRs [Berezinsky01]. These defects have to be left from the phase transitions in the early universe. The UHECRs are originated during the collapse, the annihilation or the crossings of such formations.

New hadrons

The suggestion has also been made that new neutral particles containing gluino could be producing the trans-GZK events [Farrar96]. This particle have to be stable and with lower cross-sections for the interactions during propagation. Such a particles are called "uhecrons".

Similarly vortons, superconducting cosmic strings stabilized by a current present a solution that is limited to the very highest energies.

Magnetic monopoles

The accelerated monopoles with mass < 10^{10}GeV should be the sources of UHECRs too [Porter60]. These monopoles should be accelerated in the Galactic magnetic field and then hit the Earth's atmosphere. But according to the simulations the produced showers then have to have special properties, which are not observed. Also the correlation with Galactic plane is not observed.

Violation of Lorentz symmetry presented idea of the possible departure from the strict Lorentz invariance [Coleman99]. The proposed departure is too small to be detected by the man-made accelerators, but large enough to affect the particle kinematics in ultra-high energy region and so to suppress or completely forbid the interactions of UHECRs with CMBR. Therefore the predicted cutoff in the spectrum is at least shifted by one order to higher energies and the origin of particles is possible also in the cosmological distances.

1.2 Air Shower

When a primary cosmic ray particle enters the earth's atmosphere it reacts strongly with an atomic nucleus of the air. The interaction point of the cosmic ray particle with the atmosphere is random and decided, on statistical basis, by its inelastic cross-section on the target nucleus. The inelastic cross-section, $\sigma_{\text{p-air}}$, of protons on an "air nucleus"(mean Z=7.5, mean A=14.5) is about 200mb corresponding to an interaction mean free path of ~ 80g cm^{-2} at an energy of ~10^{14}eV. So interaction occurs, on an average, at 80 g cm^{-2} from the top of the atmosphere. In this reaction a multitude of secondary particles is formed, which in turn react with atoms in the air and produce more secondary particles. This is done not only by hadronic interactions but also by the electromagnetic interactions with atoms or electrons and by the decay of unstable particles. Eventually the cascade contains thousands of hundreds of different particles which move towards the earth surface with a velocity close to the velocity of light - causing the phenomena of Extensive air shower.

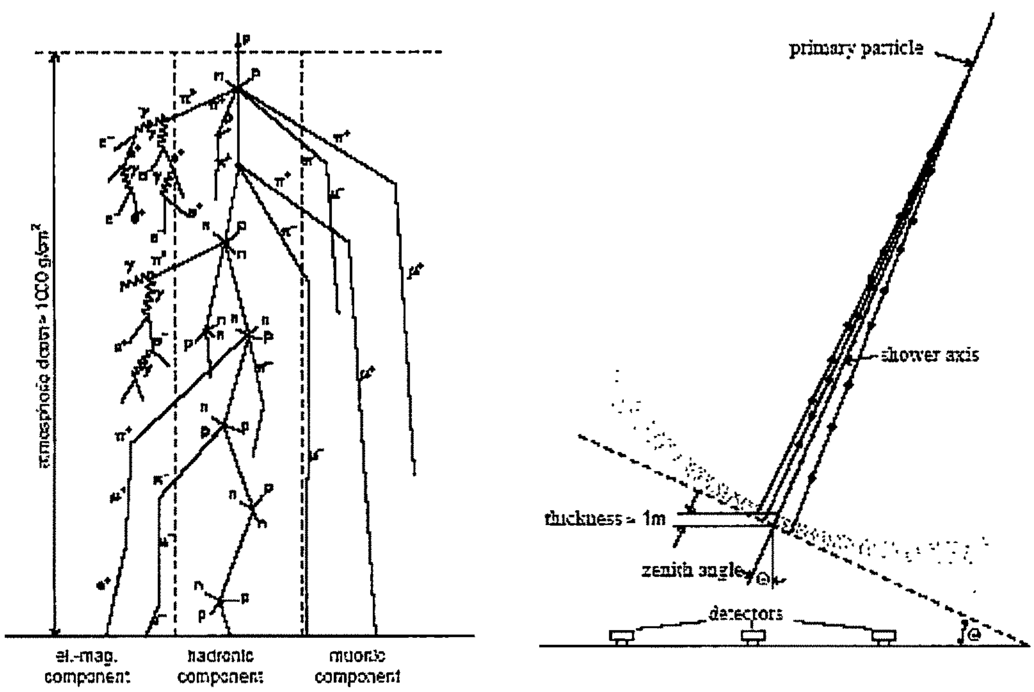

Figure 1.4 Schematic view of an extensive air shower

The particles in an EAS form a disc with a few meters thickness and up to some kilometer lateral extent as they move through the atmosphere. This disc is not completely flat, but has more the form of cone with a very obtuse opening angle. In the centre the disc is thin but as we move away from the centre thickness increases with increasing distance (as shown in figure 1.4).

The energy lost by the primary particles is shared by the secondary particles. The total number of secondary particles, known as the multiplicity, slowly increases with the energy of interaction. In the beginning of the evolution of the shower the total number of particles rises due to the continuous production of secondary particles. After the average energy per particle drops below the threshold for the production of new particles the absorption of particle in the air starts to dominate and total number drops exponential with the atmospheric depth (as shown in figure 1.5). However, muon component of EAS does not suffer significant attenuation after reaching maximum because muons lose energy only by ionization and small factions of them are lost by decay.

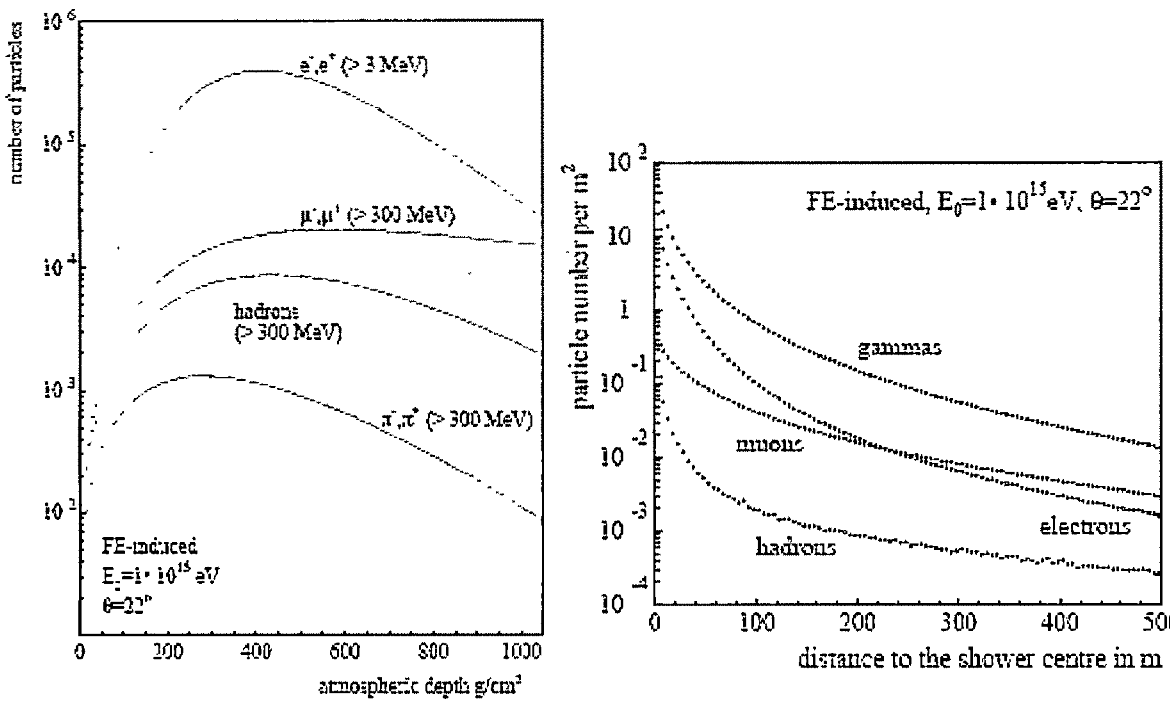

Figure 1.5 Longitudinal and lateral particle distribution in an EAS. Average over 1000 simulation of an air shower induced by a 10^{15}eV iron nucleus at a zenith angle of 22^0[Glasstetter05][Horneffer06].

1.2.1 Components of an Air Shower

The particles in an EAS can be divided into three groups- electromagnetic, hadronic, and muonic component. Neutrinos are usually not taken into account as they do not produce further secondary particles and are too difficult to measure. Similarly radiation in the UV, optical and at radio wavelength is referred to as being emitted by and not as being part of the air shower.

1.2.1.1 Electromagnetic component

The electro-magnetic component of an EAS consists of electrons, positrons and photons. It is mainly due to the decay of neutral pions into gamma photons. Though photons interact with matter causing Photo electric effect, Compton Effect and Pair production, the first two have low reaction cross-section for high energy photons and can be neglected in the formation of electromagnetic cascade of EAS. The high energy electrons produced in the pair production in turn produces gamma photon and one low energy electron by the bremsstrahlung process. Thus the electromagnetic cascade is developed by the high energy particles in which they convert into each other by pair production and bremsstrahlung. The cascade starts with no average charge but it picks up atmospheric electrons and thus develops a negative charge excess. In crossing every radiation length each particle loses 1/e fraction of its average energy. Once the energy of the electrons or positrons drops below the critical energy ($E_{c,air}$ =84.2MeV), they loose, on average, more energy by ionization than by bremsstrahlung. In this particular point the production of new photon ceases and the electromagnetic cascade dies out.

The electromagnetic cascades of hadrons initiated air shower consist of the superposition of many electromagnetic cascade whereas electron or photon initiated air shower consist of only one electromagnetic cascade.

1.2.1.2 Hadronic component

Every air shower that is initiated by atomic nuclei as primary particle starts from its hadronic component. The hadronic component consists of the strong interacting particles in the air shower, i.e. fragments of nuclei, single nucleons, mesons etc. In this process pions are the most common kind of particles. On average their transversal impulse is rather low compared to their total impulse. So, high energy hadrons are concentrated in a radius of only a few tens of meters around the shower axis. New hadrons are produced in high energy collisions of hadrons. When the energy of hadrons is too low for the production of pions it looses energy through ionization until it decays or is stopped. At the high energies of the primary particles the nucleons of a nucleus can be considered as free particles. So an iron induced air shower can be considered as the superposition of 56 proton induced air showers each with the 56th part of the total energy. The proton–air cross section above 100GeV rises only logarithmic with energy, so the iron–air interaction length is about 4 times smaller than the proton– air interaction length [Geich-Gimbel89]. This makes iron induced air showers evolve earlier and faster in the atmosphere than proton induced ones.

The integral energy spectrum of hadrons can be expressed as a power law; the spectrum is flat at lower energies and become steeper as the hadrons energy increases.

1.2.1.3 Muonic component

The muons in an air shower are produced by the decay of charged pions and kaons. The muons themselves decay into electrons/positrons and neutrinos. Compared to pions their life time is about 100 times longer. Compared to electrons the scattering and bremsstrahlung is a factor of $(m_\mu/m_e)^2 \approx 4300$ smaller. Moreover the range of the muons in the laboratory rest frame is extended by relativistic time dilation.

Hence most muons reach the earth's surface. The lateral distribution of the muons is mostly caused by the angular distribution and the height of their production. It can also be parameterized by the NKG-function [Kamata58][Greisen56]. However the latera distribution of the muons is flatter than the one of the electromagnetic component.

The energy spectrum of muons can be represented by a power law; it is flat at low energies because of increasing losses due to ionization and decay with decreasing muon energies. At higher energies the spectrum became steeper. The number of muon having energy > E_μ can be related to the shower size (N_e) and primary mass (A) by the equations (1) and (2) respectively.

$$N_\mu(>E_\mu) \;\; \infty \;\; N_e^{\alpha_\mu E_\mu} \qquad \text{-------- ----------1.2}$$

$$N_{\mu}(A) \propto A\left(\frac{N_e}{A}\right)^{\alpha_{\mu}} \propto A^{1-\alpha_{\mu}} \text{ ---------1.3}$$

The exponent $\alpha_{\mu}(E_{\mu})$ decreases with E_{μ} presumably because the decay probability of higher energy pions decreases as energy increases. The value of α_{μ} is 0.8-0.9 at E_{μ} ~ 1GeV and decreases to about 0.7 at E_{μ} ~200GeV.

1.2.2 Detection & Measurement Techniques

Earth atmosphere is acting as a large calorimeter on an incident cosmic ray and it has a vertical thickness of 26 radiation lengths and about 11 interaction lengths, which are acting in development of EAS. Based on the different phenomenon that happens to occur during its motion in the earth atmosphere and ground level, extensive air showers are detected by several different methods. Currently three differently, established methods in use to measure EAS, are as follows,

1.2.2.1 Air Čerenkov

When a fast particle moves through a medium at velocity v, greater than the phase velocity of light in that medium (so v>c/n; c is the speed of light, n is the refractive index of the given medium), it emits Čerenkov radiation. The physical principle of this effect rests in a polarization of medium by relativistically moving particle. A charged particle moving slowly through a transparent material will polarize the medium along its trajectory. The atoms around the particle are transformed into little dipoles. When the particle moves to another point, they relax to their normal state. Owing to complete symmetry of this effect no resulting field reaching larger distances is produced. However, the situation differs qualitatively along the path of flight and each element of the track is radiating. However, the elementary waves generally interfere destructively and there is then no visible effect at large distances. Only when the velocity of the particle is higher than the phase velocity of the light in the medium it will produced field detectable at distant point. Waves from the different points of the track combine constructively to form a plane wave front.

The wave fronts only add up to produce coherent radiation in a particular direction θ with respect to the velocity vectors of the particle, so the radiation should be observed only in a narrow cone along the track. The apex angle of this cone θ is given by the formula cosθ= c/vn. The intensity of radiation is given by [Longair92]

$$I(\nu) = \frac{\nu Q^2 v}{4\pi\varepsilon_0 c^3}\left(1-\frac{c^2}{n^2 v^2}\right) \quad \text{-------------------------} 1.4$$

where ν is the frequency of the emitted radiation, Q is the charge of a particle in coulombs and ε_0 is the permittivity of vacuum.

In clear, moonless nights this light can be measured by optical telescopes with photomultiplier cameras. The image obtained with this telescope shows the track of the air shower. From this track the direction of the primary particle can be reconstructed. With two telescopes observing an air shower in stereo mode one can get angular resolution on a single air showers of less than 0.1^0[Hinton04]. Since Čerenkov radiation is strongly beamed into forward direction, so the illuminated area on the ground is only few hundred meters wide. Examples are the Tunka array [Budnev05] and the AIROBICC array of the HEGRA experiment [Karle95]. The shape of the image of the air shower track is also useful to differentiate between hadron induced and photon induced air showers. Consequently this method is used for TeV-γ observatories like H.E.S.S experiment [Hinton04].

1.2.2.2 Air Fluorescence:

High energy shower particles excite and ionize the air molecules as they traverse down to the earth surface. The excited nitrogen molecules in turn emit fluorescence light mainly in the UV region (300-400nm).Most of the fluorescence light comes from 2P band system of molecular nitrogen (~80%) and 1N band system of the N_2^+ molecular ion (~20%).The emitted radiation is highly isotropic and can be detected at a large distance from the axis of the shower. By observing this light with optical telescopes one can image the track of the air shower in the atmosphere. For this reason, the whole observed sky is segmented, and each segment (typically~1^0) is observed by its own photomultiplier. The emission efficiency (ratio of emitted energy in fluorescence light to the deposited one) is poor (~1%), the detector sees the shower as a variable light bulb moving at the speed of light along the shower axis. Due to the low radiated power this method is only efficient for UHECRs. Like air Čerencov method this is only possible in clear, moonless night, i.e.-in about 10% of the time. Under favorable conditions UHECR showers should be detected at distances as large as 20km-at Fly's Eye of HiRes detectors. The fluorescence yield [Bertou00] is 4 photons per electron per meter at ground level.

The fluorescence technique is the most appropriate for energy measurements-atmosphere acts like large calorimeter and thus the emitted energy is proportional to a number of charged particles in shower.

In practice also several effects should be taken into account, which are complicating the evaluation and raising the uncertainty of result. These are, subtraction of the direct and diffused Čerenkov light, the wavelength–dependent Rayleigh and Mie scatterings and the dependence of the attenuation on the altitude.

1.2.2.3 Particle Detector Arrays

Pioneering research of Auger and his team showed that there is a relation between energy of primary particle and the size of the surface, where we are able to detect secondary particles. Primary energy above about 10^{14}eV, a large number of air shower particles have enough energy to reach earth surface. These particles can then be measured with particle detectors. The detectors are distributed uniformly over the measurement area. The spacing between two adjacent detectors determines the low energy threshold of the experiment-e.g-KASCADE array: 13m, ~$10^{14.6}$eV, and Auger 1.5km, ~$10^{18.3}$eV. [Antoni03][Kampert04], and the size of the covered area determines the highest energy at which one has a reasonable count rate, e.g. KASCADE array: 4×10^4m^2, ~ 10^{17}eV, and Auger: 3×10^9m^2, >10^{20}eV. From the arrival times of the particles in the detectors one can determine the direction of the air shower, and from the energy measured with the detectors one can get the number of particles.

'ith suitable detectors it is possible to separately measure electron and muon numbers of an r shower.

.3 Ultra High Energy Cosmic Rays (UHECRs)

Primary cosmic rays having energy above 10^{18}eV are known as UHECRs. Particles ith this energy range have unique importance because of non-existence of suitable source ıside our galaxy for accelerating upto the observed highest energy. Furthermore these ‹treme energies, about eight orders of man made accelerators, require for known methods of :celeration, extreme intensity of magnetic fields or extreme sizes of this acceleration :gions. Such conditions are hardly available at any places in the universe; may be the most ıvorable are large radio lobes in active radio galaxies. But even these need to have all ›nditions finely tuned and only in such a case the theoretically derived maximum attainable ıergy is achieving 10^{21}eV.

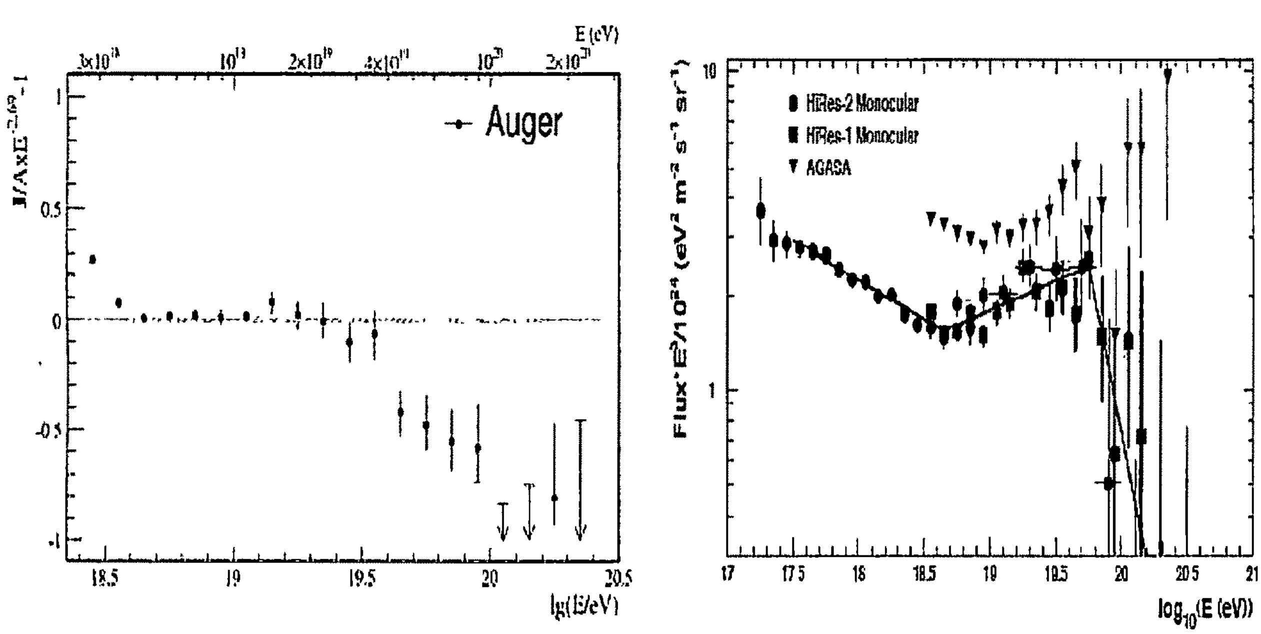

igure 1.6 Spectral deviation from E-2.09 by Auger [PAC08](left) ; flux multiplied by E3 :iRes[HiRes08] and AGASA(right)

Although the first detection of UHECRs dates back to 1962[Linsley63], it was only in the 1990s that an international effort began to address the mystery behind the UHECRs with the necessary large scale observatories. Akeno Giant Air Shower Array (AGASA) in Japan, High Resolution Fly's Eye (HiRes) at Utah,USA and the largest observatory ever constructed, the Pierre Auger Observatory in Argentina are some of the best observatories which are trying to explain the mystery of GZK cutoff , CMB etc.

In pursuing the journey to the highest energy end of UHECRs, AGASA reported an excess of flux while HiRes were closer to GZK prediction. The GZK effect is named after Greisen[Greisen66],Zatsepin, and Kuzmin[Zatsepin66] who predicted in 1966 a dramatic steepening of the spectrum above a few times 10^{19}eV caused by the interaction of UHECRs with cosmic microwave background (CMB) radiation as they propagate from extragalactic source to earth. In 2008 two observatories HiRes [HiRes08] and Pierre Auger Observatory [PAC08] published the GZK spectral feature as displayed in Fig-1.6.

This landmark measurement opens the way to astronomical searches for sources in the near by extragalactic universe using the distribution in arrival directions of trans-GZK cosmic rays. Above GZK threshold energy, sources contributing to the spectrum must lie within about 100Mpc, the so called GZK horizon or GZK sphere.The Auger AGN correlation results argues that some sources can't be much further than about 100Mpc, which rules out rare and distant sources, such as massive clusters of galaxies and most powerful radio galaxies. The Auger trans-GZK events also correlated with PSCz(Point sources Catalogue Redshift Survey) sources [Kashti08], with HI emitting galaxies [Ghiselini08], and Swift hard X-ray sources [George08].

Competing models of cosmic accelerators will be best tested once we can measure precisely the spectrum of individual sources. To do this the combination of large sky exposure and precise spectrum and composition measurements will be the best option for the cosmic ray observatories which is now feasible, limited only by the amount of exposure to each source.

1.4 Radio Emission from Extensive air Showers

Emission of Electromagnetic radiation at radio frequency due to the EAS of UHECRs has been theoretically and experimentally proved by different cosmic ray groups since 1965, when for the first time radio pulses associated with cosmic ray air showers were detected by Jelley and his co-workers in Harwell [Jelley65]. In the 1970ties the radio detection was overlooked due to the success of other methods and uncertainty about the interpretation of the radio results. The development of high resolution receiving system, new technologies as well as the advantages of this method, helped to revive its popularity among the theoretical and experimental cosmic ray groups.

Measuring the radio pulses from air showers has a number of advantages compared to the established techniques. With the RFI (radio frequency interference) suppression one can measure even in relatively radio loud environments, i.e. close to cities which are not possible with optical telescopes. It is not much affected by observing conditions. Except during thunderstorm conditions which seem to amplify the radio signal emitted by air showers [Buitink05][Buitink07] one can measure during day and night. This gives a much higher duty cycle than optical measurements.

The little attenuation of radio signals makes it possible to measure highly inclined air showers whose particle component has already, mostly died out at the ground level [Petrovic07]. This method can be used to study the air showers that are induced by high energy neutrinos, as it can help to distinguish between neutrino induced air showers and other air showers. Radio detectors can see air showers from any primary while particle detectors mainly detect those from neutrinos that had their first interaction close to the detectors [Falcke04].

The radio signal forms a continuous pulse front unlike the particle front that is quantized. This makes it possible to measure the relative arrival time of the shower front at different positions with high precision and thus get a better estimate for the arrival direction of the cosmic ray than with particle detector arrays.

1.4.1 Early Experimental Data

In 1962 Askaryan predicted that particle showers in matter should emit radio signals [Askaryan62]. He proposed that particle showers develop a negative charge excess so that the showers can coherently emit Čerenkov radiation at radio frequencies. In 1965 Jelley et.al. discovered that extensive air showers indeed produced radio pulses at 44MHz [Jelley65].In the following years emission from 2MHz up to 520MHz was found. Soon it was discovered that the signal strength in one polarization direction depends on the angle of the air shower to geomagnetic field, supporting theories that the radiation of air showers is caused by geomagnetic effects. Further studies showed that the polarization of the radio signal is consistent with geomagnetic emission process [Allan73].

The early experiments were limited by the existing technology. They restrained the observations in a relatively small band width of a few MHz. The received radio signal was integrated with a time constant of the order of hundred nanosecond to get the total receiving power. These systems hardly filter out transmitter stations that leak into the observed frequency band and thus one can't distinguish air shower pulses from RFI pulses. Consequently measurement often done at night when commercial TV and radio stations were turned off and access to the site could be restricted.

1.4.2 Recent Experiments

The first effort trying to measure radio emission from air showers with the help of fast ADCs was done by Green et. al. [Green03]. They set up one antenna near the CASA/ MIA array [Borione94] in Utah. Due to limitations of the experiment and high levels of RFI they were not able to measure radio pulses from air showers. They found an upper limit for the emission strength of 34μV/m/MHz at primary particle energy of $\sim 10^{17}$eV.

Another effort is the CODALEMA experiment [Ardouin07]. This uses several antennas of the Nancay decametric array, together with a small number of scintillation detectors. The site is very radio quiet and the scintillation detectors are well shielded. With this they are able to measure radio pulses from air showers with field strength around from a few to 25μV/m/MHz [Ardouin07]. They also confirmed the limited footprint of the illuminated area on the ground of a few hundred meters and use it to distinguish between air shower pulses and RFI pulses. One limitation of this experiment is that it does not have access to a calibration of the air shower parameters and depends on incidental measurements, e.g. estimating the primary energy from the trigger rate.

The most interesting and challenging experiment on radio detection from cosmic ray air shower is the LOPES experiment in Germany. It consists of 30 single polarization antennas that are set up at the site of the KASCADE- Grande experiment, Germany [Falcke05]. It directly samples the radio signal in the frequency range from 40- to 80 MHz and stores 0.82ms of raw data every time it was triggered by KASCADE-Grande. For the analysis the data is offline correlated with the data from KASCADE-Grande array, radio interface is digitally filtered and a beam in the direction given by the KASCADE array is formed. With this they could reliably pick out radio pulses from air showers. They found that the height of the radio pulses have nearly linear dependence on the shower size (with power index slightly smaller than one), an exponential decline with the distance of the antennas to the shower axis, and a monotonic rise with the angle of the air shower to the geomagnetic field [Horneffer06].

1.4.3 Theories

The first postulated process for radio emission from air showers was Čerenkov radiation. The particles in the air shower travel faster than the speed of light in air so they emit Čerenkov radiation. The physical size of an air shower is smaller than the wavelength at radio frequencies so the emission is coherent. In a neutral shower with as many positrons as electrons the emission from positron and electron will cancel each other. Askaryan proposed that because the atmosphere or any other matter contains many electrons but no positron an air shower develops a negative charge excess [Askaryan65]. The net charge then allows an air shower to emit Čerenkov radiation at radio wavelengths.

Another emission mechanism is due to the deflection of charged particles (mostly electrons and positrons) in the earth's magnetic field .There are two ways to look at this, both are expected to be equivalent. One interprets it as a separation of charges in the air shower which leads to transverse currents in the air shower which in turn emit dipole radiation [Kahn66]. Falcke and Gorham [Falcke03] interpreted this as synchrotron radiation of particles gyrating in the geomagnetic field.

As the experimental data shows a clear dependence of the radio emission on the angle with the geomagnetic field, the geomagnetic emission process has to be the dominant one in air showers. The field strength rises nearly linearly with the primary particle energy, this means that the emitted power rises quadratically with the primary energy. This shows that the emission is nearly totally coherent as incoherent emission would only result in a linear rise of power with energy [Huege05]. Another result obtained so far is that the total electric field strength only weakly depends on the angle of the shower to the geomagnetic field. Of course the emission is purely linearly polarized in the direction perpendicular to the magnetic field and the air shower axis. Polarization angle is dependent on the geomagnetic field – emission is linearly polarized in the direction perpendicular to the magnetic field and the shower axis. Thus showers from due north or due south are both completely east-west polarized although they have different geomagnetic angles.

Based on transition radiation, another emission mechanism is forwarded by Nishimura in 1985[Nishimura85]. When the excess negative charges from an EAS, hit the earth surface radio emission takes place due to the transition radiation mechanism. The emission is purely coherent in the low frequency region as the bunch length is very much less than the emitted wave length. The radiated field at VLF region is nearly 100 times greater than the field at LF/MF region [Dutta00][Hough73].Of course the high frequency field strength spectrum given by transition radiation resembles with the field strength spectrum according to the geo-synchrotron mechanism.

1.5 Present work

1.5.1 Motivation

Radio measurements of EAS open an entirely new window for the observation of Cosmic Rays. The technique has a number of significant benefits. Similar to the optical fluorescence technique, it allows a much more direct view into the air shower cascade than particle measurement on ground, yielding information greatly simplifying the reconstruction of air shower parameters from the particle detectors. The radio technique mainly measures quantities integrated over full evolution of the air shower. A major benefit of the radio technique is that it is not hindered by need of superb observing conditions (clear sky, moonless night, far away from any light pollution) that limits the duty cycle of fluorescence detector typically to less than 10%.

1.5.2 Work Plan

This present work is continuation of detection of UHECRs by GU miniarray [Bezboruah99]. The importance of this present work is the development of new trigger circuit for the front end electronics of GU miniarray [Saikia05][Saikia08] and the detection and measurement of radio signal associated with UHECRs [Saikia07]. The thesis of this work is organized as follows:

In chapter II we discuss the idea and theory behind the miniarray method, working of GU miniarray and finally discuss the working of newly designed Trigger Circuit (TR) for the front end electronics of GU miniarray.

In Chapter III we present the theory of transition radiation at the interface between two surfaces of different dielectric properties following Doohar approach and finally calculate the magnetic field for vacuum to medium case.

In Chapter IV we discuss the principle of small loop antenna, its electrical properties ınd behavior of multiturn loop antenna. We then discuss the simulation of loop antenna using ꞁTspiceIV and its results.

Chapter V consist of the construction, calibration and testing of receiving loop ıntenna. Then we discuss the calibration of scintillation detectors of miniarray and the ;alibration of discriminator circuits. We discuss the experimental setup for radio detection vithout miniarray and with miniarray.

Chapter VI comprises the discussion of model calculation of transition radiation using ꟳORTRAN programming language. The geometry of shower acceptance and co-ordinate ıxes are inferred.

Chapter VII consists of the experimental results of LF/ VLF detection. Power spectral lensity, electric field and pulse height distribution of received radio signal has been liscussed in this chapter.

Chapter VIII consists of the concluding remark and the future work plane.

References

[Abbasi10] R U Abbasi. *APJ Lett.,* **L64,** 731 (2010).

[Allan73] Allan & et.al. *in Proc.13th ICRC,Denver,* **4,** 2407 (1973).

[Antoni03] T Antoni & et.al. *Nucl. Instr. Meth. in Phys.Res.A,* **513,** 490 (2003).

[Ardouin07] D Ardouin & P Lautridou P., 47,no.3,, 33. *Cern Courier* **47,** 33 (2007).

[Askaryan62] G. A. Askaryan. *Soviet Phys. JETP,* **14,** 441 (1962).

[Askaryan65] G. A. Askaryan. *Soviet Phys. JETP,* **21,** 658 (1965).

[Berezinsky01] V Berezinsky, B Hnatyk and A Vilenkin. *Phys.Rev. D,* **64,** 043004 (2001).

[Berezinsky98] V Berezinsky . *arXiv: hep-ph/9802351v1* (1998).

[Bertou00] X.Bertou , M.Boratav, A.Selvon-Letessier . *Preprint astro-ph/0001516.* (2000).

[Bezboruah99] T.Bezboruah, K.Boruah and P.K.Boruah. *Astropart. Phys.,* **11,** 395 (1999).

[Bhattacharjee00] P Bhattacharjee & G Sigl. *Phys. Reports* **327**, 109 (2000).

[Blasi00] P.Blasi, R.I.Epstein and A.V.Olinto. *ApJ,* **533**, L123 (2000).

[Boldt99] E.Boldt & P. Ghosh. *Mon. Not. R. Astron. Soc.,* **307**, 491 (1999).

[Bruno01] Marco Bruno, IK0ODO. Thinking about the ideal Loops. *http://www.vlf.it* (2001).

[Budnev05] N M Budnev & et.al. *in Proc.29th ICRC,Pune* **6**, 257 (2005).

[Buitink05] S Buitink & et.al. *Proc.29th ICRC,Pune,* **00**, 101 (2005).

[Buitink07] S Buitink & et.al. *Astron. Astrophys.* **467**, 385 (2007).

[Coleman99] S.Coleman & S.L.Glashow. *Phys.Rev. D,* **59**, 116008 (1999).

[Datta00] Pranayee Datta, Runima Baishya and Kalpana Roy Sinha. *RADHEP*, 98 (2000).

[Falcke03] H Falcke & P W Gorham. *Astropart. Phys.,* **19**, 477 (2003).

[Falcke04] H Falcke, P Gorham and R J Protheroe. *New Astronomy Review,* **48**, 1487 (2004).

[Falcke05] H. Falcke & et al. *Nature* **435**, 313 (2005).

[Farrar96] G.R.Farrar . *Phys. Rev. Lett.,* **76,** 4111 (1996).

[Fermi49] E. Fermi. *Phys. Rev.,* **75,** 1169 (1949).

[Geich-Gimbel89] C. Geich-Gimbel. *Int. J Mod. Phys.,* **A4,** 1527 (1989).

[George08] M.R.George, A. C. Fabian, W. H. Baumgartner, R. F. Mushotzky and J. Tueller. On active galactic nuclei as sources of ultra-high energy cosmic rays,. *MNRAS* **388L,** 59G (2008).

[Ghiselini08] G.Ghiselini, G.Ghirlanda, F.Tavecchio and F.Fraternali. *arXiv:0806.2393* (2008).

[Glasstetter05] R Glasstetter. *Proc.29th ICRC,Pune,* (2005).

[Green03] K. Green & et.al. *Nucl. Instr. Meth.* **498** (2003).

[Green05] K. Green, J. L. Rosner, D. A. Suprun and J. F. Wilkerson. *Nucl. Instr. Meth.,* **435,** 313 (2005).

[Greisen56] K .Greisen. *Prog.Cosmic Ray Physics,* **3,** 1 (1956).

[Greisen66] K .Greisen,K .Greisen. *Phys. Rev. Lett.* **16,** 748 (1966).

[Hess12] V Hess. *Physikalische Zeitschrift* **13,** 1084 (1912).

[Hillas84] A M Hillas. *Ann. Rev. Astron. Astrophys.* **22,** 425 (1984).

[Hinton04] J. A. Hinton. *New Astronomy Review,* **48,** 331-337 (2004).

[HiRes Collaboration08] HiRes Collaboration. *Phys. Rev.Lett.,* **100,** 101101 (2008).

[Horneffer06] A.Horneffer. in .(Bonn, 2006).

[Hough73] J.H.Hough. *J.Phys A:Math.,Nucl. Gen.,* **6,** 892 (1973).

[Huege05] T. Huege & H. Falcke. Radio emission from cosmic ray air showers, Simulation results and parametrization. *Astroparticle Physics,* **24,** 116 (2005).

[Jacobsen00] Trond Jacobsen. The Russian VLF Navaid System Alpha,RSDN-20. *http://www.vlf.it* (2000).

[Jean61] A G Jean, H E Taggart and J R Wait . *J.RES.NBS-C* **3,** 65 (1961).

[Jelley65] J.V.Jelley et al. *Nature,* **205,** 327 (1965).

[Kahn66] F D Kahn & I.Lerche. *Royal Society of London Proceedings Series A* **289,** 206 (1966).

[Kamata58] K .Kamata and Nishimura J. *Prog.Theor.Phys.(Kyoto) Suppl.,* **6**, 93 (1958).

[Kampert04] K. H. Kampert et al. *Proc. XI II ISVHECRI, Pylos (Greece),* (2004).

[Karle95] A.Karle et al. *Astroparticle Physics,* **3**, 321, August (1995).

[Kashti08] T.Kashti & E.Waxman. *JCAP* **0805**, 006 (2008).

[Linsley63] John Linsley. *Physical Review Letters,* **10**, 146 (1963).

[Longair92] M.S.Longair . *High Energy Astrophysics,* (Cambridge University Press, 1992).

[Medina-Tanco] G. Medina-Tanco . *APJ Lett.,* **495**, L79 (1998).

[Nagano00] M.Nagano & A.A.Watson. *Rev. Mod.Phys.,* **72**, 689 (2000).

[Nishimura85] J Nishimura in *Proc.19th ICRC,La Jolla, USA,*308.(1985).

[PAC07] The Pierre Auger Collaboration. *Science* **318(5852)**, 938 (2007).

[PAC08] The Pierre Auger Collaboration. *Phys.Rev.Lett.,* **101**, 061101 (2008).

[Petrovic07] J Petrovic & et.al. *Astron. Astrophys.* **462**, 389 (2007).

[Porter60] N.A.Porter. *Nuovo Cimento,* **16,** 958 (1960).

[Prouza01] M Prouza (in .Charles University in Prague, 2001).

[Rudge82] A.W.Rudge & A.d.Olver and P.Knight. *The Handbook of Antenna Design* (Peter Peregrinus Ltd.,London, 1982).

[Ryu09] Dongsu Ryu, Hyesung Kang and Santabrata Das. in *31st ICRC, Lodz.*(2009).

[Saikia05] Nayanmoni Saikia, Jyoti Prasad Phukan, Subhash Chandra Rajbongshi, K Boruah and PK Boruah. *Proc.29th ICRC,Pune,* **8,** 81 (2005).

[Saikia07] Nayanmoni Saikia, Nayanmoni Saikia, Banty Tiru, PK Boruah and K.Boruah. *Indian J. of Radio & Space Phys* **36,** 436 (2007).

[Saikia08] Nayanmoni Saikia, Nayanmoni Saikia, Banty Tiru, Dudumoni Handique, PK Boruah and K Boruah. *Indian J.Phys* **82(5),** 627 (2008).

[Shaviv05] N J Shaviv. *Journal of Geophysical Research (Space Physics)* **110**, 8105 (2005).

[Stanev95] T. Stanev, P. Biermann, J. Lloyd-Evans, J. Rachen and A.A.Watson . *Phys.Rev.Lett.,* **75,** 3056 (1995).

[**Stecker01**] F.W.Stecker . *Preprint astro-ph/0101072 v2* (2001).

[**Takahara96**] F Takahara. *Proceeding of the International Symposium on Extremely High Enegry Cosmic Rays, University of Tokoy*, 61 (1996).

[**Takeda99**] M. Takeda & et.al. *ApJ,* **522**, 225 (1999).

[**Uchihori00**] Y.Uchihori et al. *Astropart. Phys.,* **13**, 151 (2000).

[**Veron-Cetty06**] M.-P. Veron-Cetty & P.Veron. *Astron. Astrophys.* **455**, 773 (2006).

[**Waston06**] A. Watson. *Nucl. Phys. Proc. Suppl.,* **151,** 83 (2006).

[**Watson92**] A.A.Watson. *Nucl.Phys.B(Proc.Suppl.),* **28,** 3 (1992).

[**Waxman95**] E.Waxman . *Phys. Rev. Lett.,* **75**, 386 (1995).

[**Zatsepin66**] G T Zatsepin & V A Kuzmin. *JETP Lett.* **4** (1966).

CHAPTER II

The Mini-Array Method

2.1 Introduction

The main difficulty in studying the highest energy cosmic rays is their extremely low intensity. Instead of gathering all the available resources in one place (e.g. AGASA, HiRes, Pierre Auger, KASCADE), John Linsley suggested [Linsley83], a way to solve the problem at much less cost per unit sensitive area: the use of numerous inexpensive miniarray operating independently of each other having small dimension compared with the distance to the axes of the studied showers. They can operate anywhere, even in the cities and in addition to the quantities usually observed miniarray records shower particles arrival time distribution.

The particles making up an air shower travel in a swarm which is remarkably compact near the shower axis. Within 10m of the axis the thickness is only a meter or two [Bassi53]. But when the thickness is measured at a great distance it is much greater, tens to hundred meters [Linsley62].The Linsley effect is the increase in spread of arrival times in the particle sample from a given shower with increasing distance from the shower centre. Thus, the measured time spread of the particles striking localized detector system gives the value of impact parameter(r) at the detector level and the number of striking particles gives the local particle density(ρ).The shower size (N) is estimated from the assumed lateral distribution function. Thus the primary energy (E) is computed.

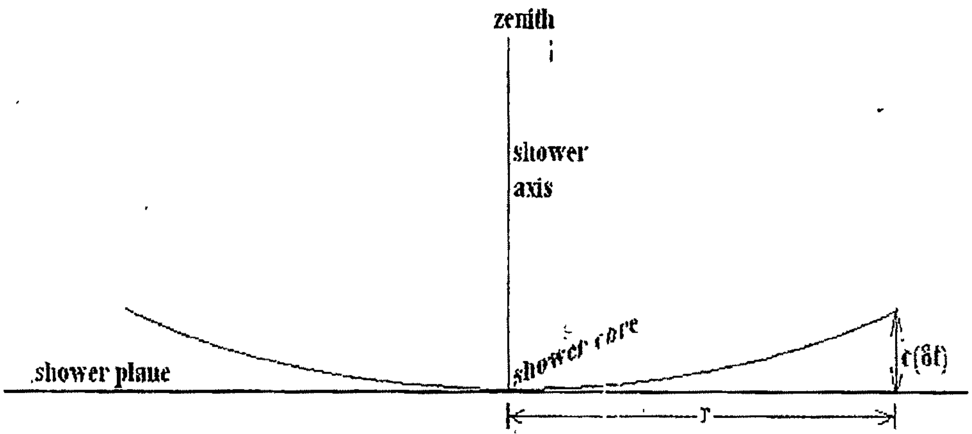

Figure2.1 Geometrical Parameters of a vertical EAS. r is the distance from shower core to the measured point and δt is the time delay.

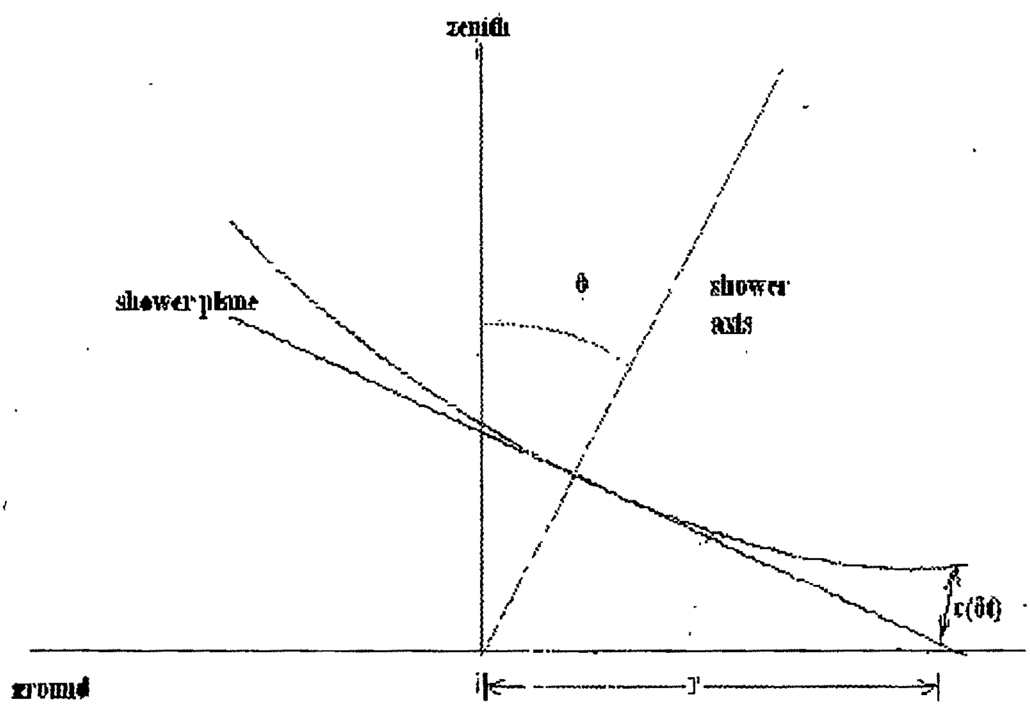

Figure2.2 Geometrical Parameters of an inclined EAS, r is the distance from shower core to the measured point and δt is the time delay.

The relation between the shower disc thickness σ (ns) to the impact parameter has been derived by Capdevielle et al. [Capdevielle03] from their simulation with CORSIKA for near vertical shower and is given by

$$\sigma_t(r) = 2.6\left(1+\frac{r}{25}\right)^{\beta} \text{-----------------------} 2.1$$

Where β=1.4 and derived from experimental data.

The purpose of miniarray is to scan the largest possible area consistent with a given uncertainty. The core of the EAS should fall up to a maximum distance determined by the minimum detected particle number that gives a tolerably small uncertainty.
Designing of miniarray in the study of EAS by using Linsley effect must include the calculation of the expected rates. The results will guide to choose the detectors and their placement. Detailed calculations are given in [Hazen85] and the conclusion states that it is necessary to go down to low particle densities (large detection areas), in order to get a good rate for high energy showers. However, a too low particle density would simply imply a large amount of statistical fluctuations and a large accidental rate. Hence a tradeoff must be reached.

Another most important factor in studying EAS using miniarray is that the hardware trigger should be carefully designed so that a minimum value of the time spread is imposed. This reduces triggers by showers with less impact parameter (too small time spread). The triggers from low energy showers are also eliminated by imposing the minimum particle number within the time spread.

2.2 Theoretical estimation From Miniarray Geometry

The particle density distribution for large shower and medium core distance ($100<r<1000$m) has been parameterized by using our simulated miniarray data for proton and iron initiated showers separately as follows:

$$\rho(N,r) = \varepsilon N r^{-n} \text{-----------------------} 2.2$$

Where ε = 0.00053, N = Shower size and n=1.5 for proton primary as deduced by reanalysis of miniarray data using CORSIKA simulation [Goswami05]

The differential and integral shower size spectrum [Bezboruah99] is respectively,

$$j(N) = -\gamma D N^{-(\gamma+1)} \quad \text{-------------------------}2.3$$

$$J(N) = D N^{-\gamma} \quad \text{-----------------------------}2.4$$

Where the constants have values D=318 & $\gamma = 1.7$

From the above relations we can derive the frequency of Linsley's event as a function of minimum time spread (σ_l) and threshold density (ρ_l) and shower size N , as

$$F(>\sigma_l, >\rho_l) = \int_{N_{min}}^{\alpha} A(N) j(N) dN \quad \text{----------------------}2.5$$

$$F_L(N) = \int_{N}^{\alpha} A(N) j(N) \quad \text{-----------------------------------}2.6$$

Where $A(N) = \pi(r^2_{max} - r^2_{min})$ ------------------------2.7

Here A(N) is the acceptance area, an annular ring whose inner radius is determined by the minimum time spread (σ_l) and outer radius is determined by density threshold $\rho_l = 1.5m^{-2}$ selected.

The values of r_{min} & r_{max} are deduced from equations 2.8 and 2.9 respectively as ,

$$r_{min} = \left(\frac{\sigma_1}{2.6}\right)^{1/\beta} \quad \text{--------------------------------}2.8$$

$$r_{max} = \left(\frac{CN}{\rho_1}\right)^{1/n} \quad \text{---------------------------------}2.9$$

The minimum detectable shower size is given by the condition,

$A(N_{min}) = 0$

This gives

$$N_{min} = \left(\frac{\rho_1}{\varepsilon}\right)\left[C\left\{\left(\frac{\sigma_1}{2.6}\right)^{1/\beta} - 1\right\}\right]^{n} \quad \text{---------------}2.10$$

2.3 Recent miniarray Experiment

CHICOS (California High School Cosmic Ray Observatory) [Lynn05][McKeown05][McKeown03] is deploying over 180 scintillation detectors at 90 school sites to form an array with area of more than 400 km^2 in the San Gabriel and San Fernando Valley of southern California. Each site consists of two scintillation detectors with a computer to acquire data, and operates in an autonomous mode using GPS time-stamping of events. The data from each site is transmitted via internet to a central computer at Caltech where the data is logged, analyzed, and accessible to the high schools. With a detectable energy range of 10^{18}-10^{21}eV CHICOS aims to provide data related to the flux and distribution of arrival directions of UHECRs.

HiSPARC (High School Project on Astro-Physics Research With Cosmic Rays) [Timmenmans05][Holten05] in Netherlands, ALTA(Alberta Large-area Time-coincidence Array) [Brouwer05][Pinfold03] in Canada, ROLAND MAZE Project [Maze06] in Poland, LAAS(Large Area Air Shower) experiment [Ochi01][Ochi05] in Japan and SCROD(School Cosmic Ray Outreach Detector) experiment[Scrod10] in Boston, USA are also detecting UHECRs using miniarray method. Among all of these miniarrays, SCROD gets a special technological feature by using APD (Avalanched Photo Diode) to collect the light produced in scintillators instead of normal photomultiplier tube. APDs have higher quantum efficiency than the traditional photomultiplier tubes. They are mechanically robust and easy to use.

2.4 GU Miniarray

GU Miniarray, a particle detector array is an assembly of eight plastic scintillation counters placed side by side at the rooftop of Physics building of Gauhati University (26°10′ N, 91°45′E and altitude 51.8m) covering a total carpet area of 2m^2.Each detector unit consists of a plastic scintillation block (size $50 \times 50 \times 5$ cm^3) having polyvinyltoluene base (with resolution 20% and decay time 4ns), a fast photomultiplier tube (EMI 9807B) and a preamplifier. Signals from each detector are fed to the miniarray lab via 100m RG 58U co-axial cable.

UHECRs have been continuously detected by GU miniarray since 1996 for a period of 14 years. These data were analyzed and results were found to be consistent with other groups, e.g-AGASA, Yakutsk etc. These data once again analyzed using CORSIKA [Goswami05].The results were again compared with the data of world wide cosmic ray groups. The over all slope of differential energy spectrum calculated with CORSIKA for proton in the energy range of $10^{17.0}$-$10^{19.0}$eV was (-2.369 ± 0.075) and for iron in the energy range of $10^{17.0}$-$10^{19.4}$eV was (-2.207 ± 0.067) as shown in firgure2.3.

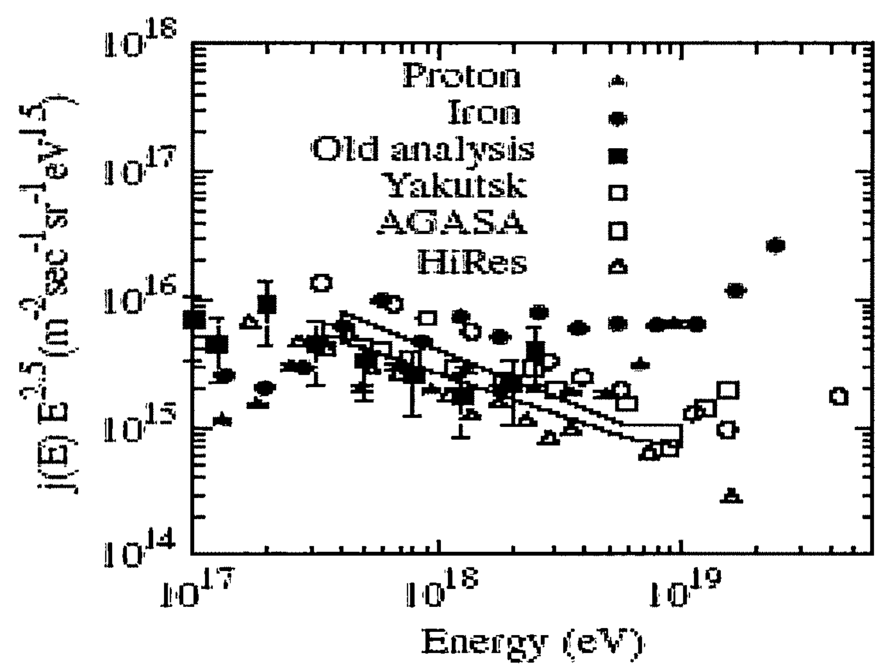

Figure2.3 Miniarray differential energy spectrum [Goswami05].The differential flux is multiplied by $E_o^{2.5}$. Data for proton and iron are obtained from reanalysis of experimental data using CORSIKA assuming proton and iron as primary Cosmic Ray particles. Region between solid lines give the flux as compiled from Akeno and Havarah Park data by Nagano and Watson (2000)[Ave01]

Moreover, the following conclusion had been drawn by U. D. Goswami at.el. [Goswami05]-

1. New analysis gives estimates of primary energy significantly higher than previous analysis. Energy spectrum after reanalysis is found to span from 10^{17}eV to 10^{19}eV for

proton primary and from 10^{17}eV to $10^{19.4}$eV for iron primary and further confirms the irregular behavior of energy spectrum at ultra high energy region with a prominent dip;

2. The differential energy spectrum shows structure similar to that observed by other world groups. Spectral breaks are found to occur at higher energies compared with earlier analysis. The spectrum becomes steeper around $10^{17.5}$eV and $10^{17.7}$eV and flattens around $10^{18.7}$ and $10^{19.1}$eV for proton and iron primaries, respectively forming a dip. Earlier analysis showed a dip around $10^{18.2}$eV. Comparisons of different features with other world data are shown in Table2.1 [Goswami05] and Table2.2 [Goswami05];

Table 2.1 A comparison of slope before the dip of the differential energy spectrum

Experiment	Slope before the dip	Energy range (eV)
Yakutsk	-3.195 ± 0.009	$10^{17.5}$-$10^{19.2}$
AGASA	-2.981 ± 0.058	$10^{17.6}$-$10^{18.9}$
HiRes-I	-3.185 ± 0.059	$10^{17.2}$-$10^{18.5}$
GU Miniarray(old analysis)	-3.468 ± 0.131	$10^{17.4}$-$10^{18.2}$
GU Miniarray(new analysis, p)	-2.733 ± 0.094	$10^{17.5}$-$10^{18.7}$
GU Miniarray(new analysis, Fe)	-2.538 ± 0.081	$10^{17.7}$-$10^{19.1}$

Table2.2 A comparison of overall slope of the differential energy spectrum

Experiment	Slope before the dip	Energy range (eV)
Yakutsk	-3.03 ± 0.047	$10^{17.5}$-$10^{19.2}$
AGASA	-2.884 ± 0.059	$10^{17.6}$-$10^{19.2}$
HiRes-I	-3.151 ± 0.036	$10^{17.2}$-$10^{19.2}$
GU Miniarray(old analysis)	-2.938 ± 0.108	$10^{17.0}$-$10^{18.8}$
GU Miniarray(new analysis, p)	-2.360 ± 0.075	$10^{17.0}$-10^{19}
GU Miniarray(new analysis, Fe)	-2.207 ± 0.067	$10^{17.0}$-$10^{19.4}$

3. There is a significant difference between spectra predicted by pure proton and pure iron assumptions. However, proton assumption results agree more with Nagano and Watson compilation [Ave01] within spectral range from $10^{17.5}$eV to $10^{18.5}$eV. Beyond 10^{19}eV results of different giant arrays are found to be contradictory;

4. Differential energy spectrum corresponding to best least square fit in the energy region $10^{17.0}$-$10^{19.0}$ eV is derived as $j(E_0)= j_0 E_0^{-p}$, where for proton primary $j_0 = 7.107 \times 10^{12}$ & p= 2.360 ± 0.075 and for iron primary $j_0 = 2.772 \times 10^{10}$ & p= 2.207 ± 0.067;

5. A relatively higher flux is seen for both proton and iron beyond the dip, as compared with the other world data.

2.4.1 Experimental Set-up

Figure 2.4 shows the block diagram of the experimental set-up of GU miniarray. All signals from the miniarray hut are coursed to the miniarray lab via 100m RG 58U co-axial cable. In the miniarray lab, signals from each detector are first discriminated with a lower discrimination level 60mV to get the logic level. The out put of each eight discriminators are order to detect UHECR's EAS we assigned a maximum time spread of 2.5μs. Thus if we ve at least two particles within the time window 2.5μS we record the data for further alysis.

1.3 Trigger Circuit

The trigger unit is one of the most important parts of the data acquisition system of niarray lab. The trigger circuit is used to select data which is from a genuine EAS event d to reject all other data coming from other sources. The requisite criteria to record coming pulses from the miniarray are that there should be minimum two pulses within iuS. The incoming pulses are monitored by the trigger circuit and whenever it receives two more than two pulses within 2.5uS it produces trigger pulse. Once the recording DSO ceives the trigger pulse it start recording the corresponding pulses for which the trigger is nerated. The designing of the trigger circuit is a part of my work and the performance of circuit is discussed here.

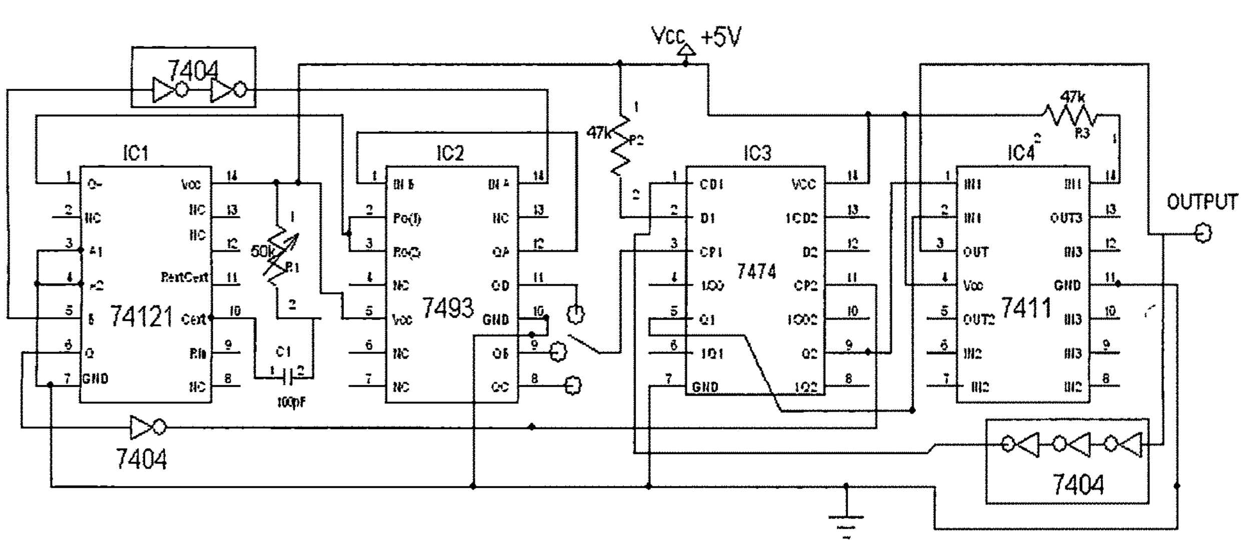

Figure 2.5 Schematic diagram of Trigger Circuit

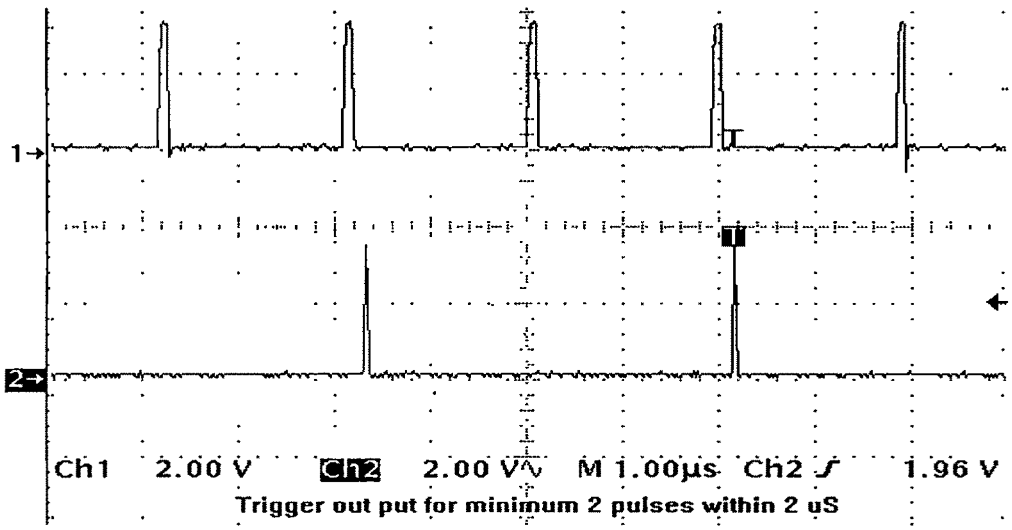

Figure 2.7 Trigger out put for minimum 2 pulses within 2µS

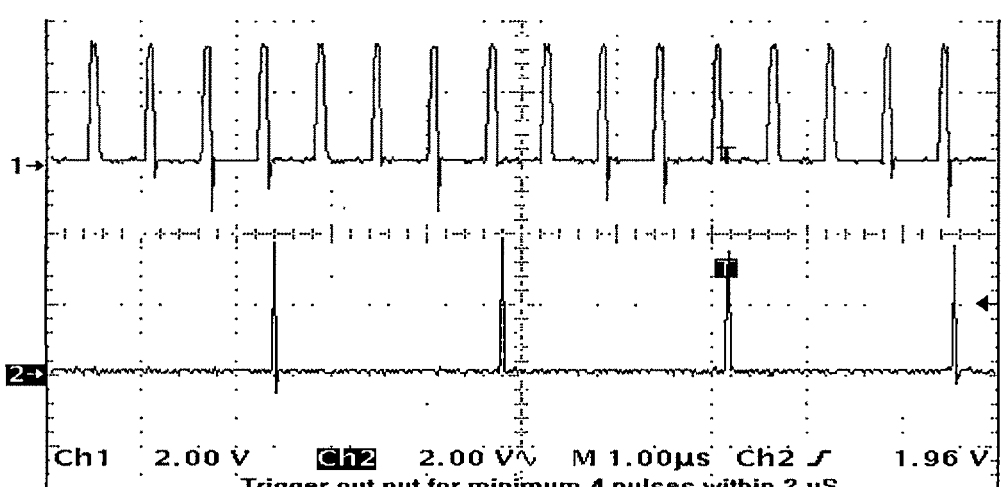

Figure 2.8 Trigger out-put for minimum 4 pulses within 2µS .

The following results are noted:

References

[Ave01] M.Ave et.al. *27th ICRC,Hamberg,Germany* **1**, 381 (2001).

[Bassi53] P.Bassi,G. Clark and B.Rossi. *Phys. Rev.,* **92**, 441 (1953)

[Bezboruah98]T.Bezboruah, K.Boruah and P.K.Boruah. *Nucl. Instr. Meth. in Phys.Res.,* **A410**, 206 (1998).

[Bezboruah99]T.Bezboruah, K. Boruah and P.K. Boruah. *Astropart. Phys.,* **11**, 395 (1999).

[Brouwer05] W.Brouwer, W.J.Burris, B.Caron, J.Hewlett, L.Holm, A.Hamilton, W.J.McDonald, J.L.Pinfold, P.Price, J.R.Schaapman, L.Sibly, R.A.Soluk, L.J.Wampler. *Nucl. Instr. Meth. in Phys.Res.,* **A539**, 595 (2005).

[Capdevielle03] J.N.Capdevielle et. al. in *Proc.28th ICRC,Tsukuba, Japan* ,217.(2003).

[Goswami05] U.D.Goswami, K., P.K. Boruah, T. Bezborah. *Astropart. Phys.,* **22**, 421 (2005).

[Hazen85] W.E.Hazen. *Proceeding-28th ICRC* **HE4.7-8**, 339 (1985).

[Holten05] J.W.van Holten. HiSPARC a view from bottom,. *HiSPARC Report* (2005).

[Linsley62] J.Linsley and L.Scarsi. *Phys. Rev.,* **128**, 2384 (1962).

1. The circuit worked successfully with the pulsing unit.
2. Selection could be made according to the desired number (2, 4, and 8) of pulses per stipulated time. The desired number of pulses can be selected with a slight modification of the circuit.
3. Good noise immunity is achieved due to the use of logic circuit element.

2.4.3.3 Simulation with VHDL (Very high speed Integrated Circuit Hardware Description Language)

We model the new trigger circuit using VHDL [ModelSim08] in the Top Level Behavioral Model. The block diagram of the model IC is shown in Figure 2.9. The Clock frequency in this simulation is 10 MHz which is very high compared to the frequency of secondary UHE Cosmic Ray particle in the ground level.

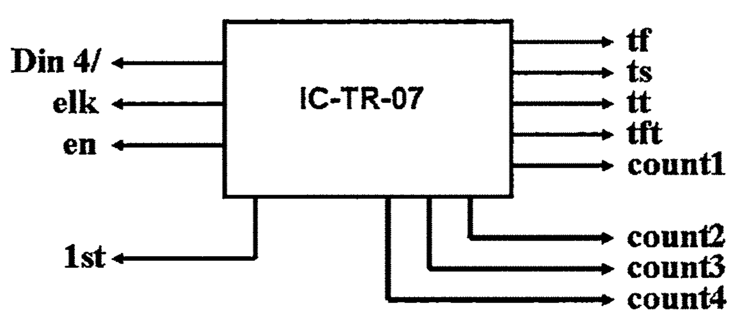

Figure 2.9 Block Diagram of the simulated circuit

The simulation is done only for 4 outputs corresponding to 4 input conditions. The 4 inputs are fixed at 2, 3, 4, 5 particle pulses within the 2.5µs time window .Output tf corresponds to the condition when there are only 2 particle pulses in the input , output ts corresponds to 3 incoming pulses, output tt corresponds to 4 incoming pulses and output tft corresponds to the 5 incoming pulses within 2.5µs time window. Moreover each output is connected with an up counter which counts the number of output pulses. One snapshot of the simulation is shown in Figure 2.10

[Linsley83] J.Linsley. *Research Report UNML-6/20/83* (1983).

[Lynn05] T.W.Lynn, E.Brobeck, B.E.Carlson, C.J.Jillings, M.B.Larson, R.D.McKeown, J.E.Hill, B.J.Falkowaski, R.Seki, J.Sepikas, G.B.Yodh, D.Wells, K.C.Chan. *Proceeding-29th ICRC*, 101 (2005).

[Maze06] http://maze.u.lodz.pl/mazeeng.htm

[McKeown03] R.D.McKeown, B.E.Carlson, C.J.Jillings, M.B.Larson, T.W.Lynn, J.E.Hill, B.J.Falkowski, R.Seki, J.Sepikas and G.B.Yodh. *Proceeding-28th ICRC*, 1057 (2003).

[McKeown05] R.D.McKeown, B.E.Carlson, C.J.Jillings, M.B.Larson, T.W.Lynn, J.E.Hill, B.J.Falkowski, R.Seki, J.Sepikas, G.B.Yodh. *Proceeding 29th ICRC* **6**, 377 (2005).

[ModelSim08] ModelSim SE 5.7g, e. v., available from http://www.mentor.com. in (2008).

[Ochi01] N.Ochi, T. W., Y. Yamashita, I.Yamamoto, T. Nakatsuka. *Nucl.Phys.B(Proc.Suppl.),* **97**, 165 (2001).

[Ochi05] N.Ochi, A.Iyono, T.Konishi, T.Morita, T.Nakatsuka, C.Noda, S.Ohara, K.Okei, M.Okita, J.Ryou, N.Takahashi, M.Tokiwa, S.Tsji, T.Wada, I.Yamamoto, Y.Yamashita. *Proceeding-29th ICRC* **6**, 201 (2005).

[Pinfold03] J.L.Pinfold et.al. *ICATPP* **108** (2003).

[Scord10] http:/www.hepnt.physics.neu.edu/scrod

[Timmermans05] C.Timmermans-HiSPARC Collaboration. *Proceeding-29th ICRC* **6**, 345 (2005).

CHAPTER III

Transition Radiation

A charged particle moving through a medium in a straight line with a constant velocity v in time can radiate energy only when the velocity of the source is greater than the phase velocity of light in that medium. This radiation, with its characteristic angle of emission, $\theta_c=\sec^{-1}(\beta\varepsilon^{1/2})$, is Čerenkov radiation. If the medium is not homogeneous and/ or varies with time then in such a medium or near it the situation is different. Under such conditions, a source can emit transition radiation. This new radiation, first noted by Ginzburg and Frank in 1946[Ginzburg46][Ginzburg80], is defined as the radiation emitted by a charge (or any other source without any intrinsic frequency) moving uniformly along a straight line under inhomogeneous conditions - an inhomogeneous medium, in a medium changing with time or near such a medium .

The simplest problem of this type concerns a charge crossing the boundary between two medium. Far from the boundary in the first medium the particle has certain field's characteristic of its motion and of that medium. Later, when it is deep in the second medium, it has fields appropriate to its motion and that medium. Even if the motion is uniform throughout, the initial and final fields will be different if the two media has different electromagnetic properties. Evidently the fields must reorganise themselves as the particle approaches and passes through the interface. In this process of reorganization some part of the fields are shaken off as transition radiation.

The calculation of transition radiation for the case of two dielectric media was first carried out by Beck [Beck48]. His approach was to use the method of images for finding the field of the particle in the two media and then to introduce the transition radiation field in order to satisfy a boundary condition on the field with time.

The same case was subsequently treated by Garibian [Garibian58] in his search for wave solutions in the radiation zone. Garibian then went on to solve a boundary value problem with the fields expanded in plane incoming and outgoing waves. Other aspects of transition radiation have also been considered in the literature. Pafomov [Pafomov58], Garibian & Chalikian [Garibian59] considered the case of transition radiation in a slab. Garibian's method was later used by Dooher [Dooher71] to calculate Transition radiation from magnetic monopoles. Recent work by Saveliev [Saveliev02] has led to the development of a theoretical description of transition radiation in the prewave zone, i.e. close to the trajectory of the incident charged particle.

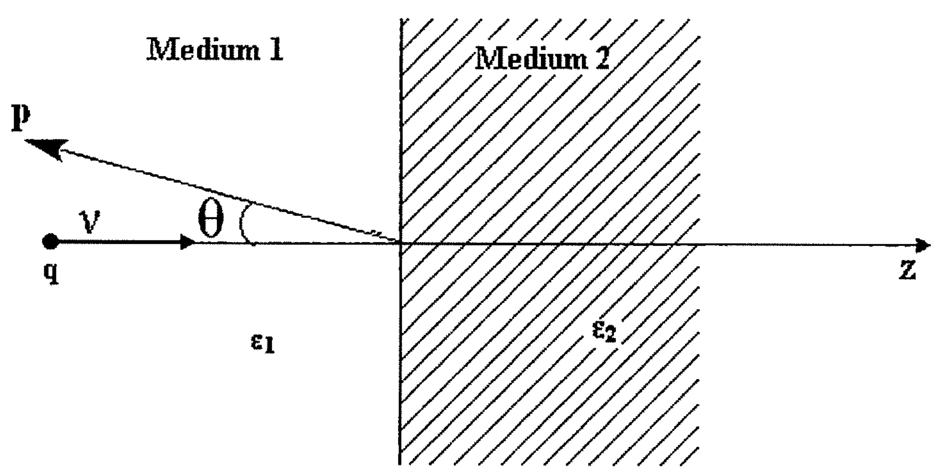

Figure 3.1: A schematic diagram of transition radiation emitted from a charge q moving with velocity v along z axis, normally incident upon the boundary between vacuum and a conductor of dielectric constant ϵ_2. P denotes the point of observation and θ is the angle at which transition radiation is emitted at frequency of ω.

3.1 Theory of transition radiation

We discuss the transition radiation field of a charged particle moving through the interface between two media following Doohar's [Doohar71] approach. The problem is to obtain the solution of Maxwell's equation for the two regions 1& 2, considering a point charge q moving with a constant velocity v along the z direction, crossing the boundary plane z = 0 at t =0 as shown in Figure 3.1. The first step is to resolve the relevant fields into Fourier Components with respect to time. This approach is adopted from [fermi40]

$$\left(\vec{E},\vec{H},\vec{D},\vec{B}\right)=\int d\omega e^{-i\omega t}\left(\vec{E}_{\omega},\vec{H}_{\omega},\vec{D}_{\omega},\vec{B}_{\omega}\right)\text{---------}3.1$$

Where $\vec{E}$ *and* $\vec{D}$, $\vec{B}$ *and* $\vec{H}$ are related by the following relations

$$\left.\begin{aligned}\vec{D}_{\omega}&=\varepsilon(\omega)\vec{E}_{\omega}\\ \vec{B}_{\omega}&=\mu(\omega)\vec{H}_{\omega}\end{aligned}\right\}\text{---------------}3.2$$

By using the particle current density $\vec{j}$, given by $\vec{j}=e\vec{v}\delta\left(\vec{X}-\vec{v}t\right)$ the Maxwell's equations for region 1,2 as

$$\nabla\times\vec{H}_{\omega1,2}=\frac{-i\omega}{c}\varepsilon_{1,2}\vec{E}_{\omega1,2}+\frac{2e\vec{n}_z}{c}e^{i(\omega/v)z\delta(\vec{\rho})}\text{------------------------}3.3$$

$$\nabla\times\vec{E}_{\omega1,2}=\frac{-i\omega}{c}\mu_{1,2}\vec{H}_{\omega1,2}\text{--}3.4$$

$$\nabla\cdot\vec{E}_{\omega1,2}=\frac{2e}{v\varepsilon_{1,2}}\delta\left(\vec{\rho}\right)e^{i(\omega/v)z}\text{--}3.5$$

$$\nabla\cdot\vec{H}_{\omega1,2}=0\text{--}3.6$$

Where $\vec{X}=\vec{\rho}+z\vec{n}_z$

Resolving the field vectors into Fourier components with respect to the transverse displacement vector $\vec{\rho}$ we get the following equation;

$$\left(\vec{E}_{\omega},\vec{H}_{\omega},\vec{D}_{\omega},\vec{B}_{\omega}\right)=\int d^2\kappa e^{-i\vec{\kappa}.\vec{\rho}}\left[\vec{E}_{\omega}\left(\vec{\kappa},z\right),\vec{H}_{\omega},\vec{D}_{\omega},\vec{B}_{\omega}\right]\text{------------------}3.7$$

Thus equations (3.3-3.6) become

$$\left[i\vec{K}+\vec{n}_z\frac{\partial}{\partial z}\right]\times\vec{H}_{\omega 1,2}=\frac{-i\omega}{c}\varepsilon_{1,2}\vec{E}_{\omega 1,2}+\frac{2e\vec{n}_z}{2\pi^2 c}e^{i(\omega/v)z} \text{------------------------}3.8$$

$$\left[i\vec{K}+\vec{n}_z\frac{\partial}{\partial z}\right]\times\vec{E}_{\omega 1,2}=\frac{i\omega}{c}\mu_{1,2}\vec{H}_{1,2} \text{--}3.9$$

$$\left[i\vec{K}+\vec{n}_z\frac{\partial}{\partial z}\right]\cdot\vec{E}_{\omega 1,2}=\frac{e}{2\pi^2 v\varepsilon_{1,2}}e^{i(\omega/v)z} \text{-------------------------------------}3.10$$

$$\left[i\vec{K}+\vec{n}_z\frac{\partial}{\partial z}\right]\cdot\vec{H}_{\omega 1.2}=0 \text{---}3.11$$

The general solution of equations (3.8-3.11) can be written as the sum of a particular solution (particle field), denoted by the superscript p, and a homogeneous solution (the radiation field), denoted by a prime. It is clear that the particle fields must be of the form

$$\left(\vec{E}^p_\omega,\vec{H}^p_\omega,\vec{D}^p_\omega,\vec{B}^p_\omega\right)=\left[\vec{e}^p_\omega,\vec{h}^p_\omega,\vec{d}^p_\omega,\vec{b}^p_\omega\right]e^{i(\omega/v)z} \text{----------------------------}3.12$$

With the wave vector of the particle field $\vec{k}$, defined by

$$\vec{K}=\vec{k}+\frac{\omega}{v}\hat{n}_z \qquad \text{---}3.13$$

Using equations 3.12 & 3.13, Maxwell's equations (3.8-3.11) are transformed into a set of algebraic equations, which can be solved easily. The homogeneous equations are transformed into a wave equation of the form $\left(\frac{d}{dz^2}+\lambda_{1,2}{}^2\right)(E'_\omega,H'_\omega)=0$ ----3.14

where $\lambda^2=\frac{\omega^2}{c^2}\chi-k^2, \quad \chi=\varepsilon\mu$ ----------------------------------3.15

The homogeneous solutions are obtained by utilizing continuity conditions at $z=0$ and it can be shown that the components E'_ϕ and H'_ρ are zero.

The Poynting vector in the direction of the radiation field wave vector is given by

$$S_R=\frac{C}{4\pi}(H'_\phi E'_z\sin\theta+H'_\phi E'_\rho\cos\theta) \text{------}3.16$$

The components of radiation fields in the wave zone is expressed in terms of Bessel function

$$E'_{1\rho} = \frac{-e}{\pi v}\iiint \frac{k^2\lambda_1\eta_1}{\zeta} J_1(\rho k)dkd\omega \times e^{-i\lambda_1 z - i\omega t} \text{ ------------------------------3.17}$$

where

$$\zeta = \lambda_2\varepsilon_1 + \varepsilon_2\lambda_1 \text{ ------------------------------3.18}$$

$$\eta_1 = \frac{\varepsilon_2/\varepsilon_1 - (v/\omega)\lambda_2}{\kappa^2 - \chi_1\omega^2/c^2} + \frac{-1+\left(\frac{v}{\omega}\right)\lambda_2}{\kappa^2 - \chi_2\omega^2/c^2} \text{ ------------------------------3.19}$$

In terms of radial distance R and angle θ,

$$\left.\begin{aligned} z &= -R\cos\theta \\ \rho &= R\sin\theta \end{aligned}\right\} \text{ -----------------3.20}$$

Finally,

$$E'_{1\rho} = \frac{e\beta^2}{\pi v R}\sin\theta\cos^2\theta\int d\omega\; e^{iR(\omega/c)\sqrt{\chi_1} - i\omega t}\chi_1^{3/2}\xi_1 \text{ ---------3.21}$$

$$E'_{1z} = \frac{e\beta^2}{\pi v R}\sin^2\theta\cos\theta\int d\omega e^{iR(v/c)\sqrt{\chi_1} - i\omega t}\chi_1^{3/2}\xi_1 \text{ ----------------------3.22}$$

$$H'_{1\varphi} = \frac{e\beta^2}{\pi v R}\sin\theta\cos\theta\int d\omega e^{iR(v/c)\sqrt{\chi_1} - i\omega t}\mu_1\varepsilon_1{}^2\xi_1 \text{ ---------------------3.23}$$

where

$$\xi_1 = \frac{(\varepsilon_2/\varepsilon_1 - 1)[1+\beta(\chi_2 - \chi_1\sin^2\theta)^{1/2} - \beta^2\chi_1] - \beta^2\varepsilon_2\mu_1(\mu_2/\mu_1 - 1)}{[\varepsilon_1(\chi_2 - \chi_1\sin^2\theta)^{1/2} + \varepsilon_2\sqrt{\chi_1}\cos\theta](1-\beta^2\chi_1\cos^2\theta)[1+\beta(\chi_2 - \chi_1\sin^2\theta)^{1/2}]} \text{ ---- 3.24}$$

3.1.1 Vacuum to medium case:

For the vacuum to medium case,

$\epsilon_1 = \mu_1 = \mu_2 = 1$, $\epsilon_2 = \epsilon$

And for extremely relativistic particles,

$' = \frac{v}{c} = 1$

/ith all these substitutions equation (3.24) simplifies to-

$$_1 = \frac{(\varepsilon-1)[(\varepsilon-\sin^2\theta)^{1/2}]}{[\varepsilon-\sin^2\theta)^{1/2}+\varepsilon\cos\theta]\sin^2\theta\,[1+(\varepsilon-\sin^2\theta)^{1/2}]} \quad \text{------------3.25}$$

ınd equation (3.23) simplifies to-

$$I'_{1\varphi} = 1.06\times10^{-27}\times\frac{\sin\theta\cos\theta}{R}\times\frac{(\varepsilon-1)[(\varepsilon-\sin^2\theta)^{1/2}]}{[\varepsilon-\sin^2\theta)^{1/2}+\varepsilon\cos\theta]\sin^2\theta[1+(\varepsilon-\sin^2\theta)^{1/2}]}\times\int d\omega e^{iR(\omega/c)-i\omega t}$$

------------------------3.26

'his integral in the above equation is a delta function

$$\int d\omega e^{iR(\omega/c)-i\omega t} = \delta(\frac{R}{c}-t)$$

'hus

$$I'_{1\varphi} = 1.06\times10^{-27}\times\frac{\cot\theta}{R}\times\frac{(\varepsilon-1)[(\varepsilon-\sin^2\theta)^{1/2}]}{[\varepsilon-\sin^2\theta)^{1/2}+\varepsilon\cos\theta]\,[1+(\varepsilon-\sin^2\theta)^{1/2}]}\times\delta(\frac{R}{c}-t)$$

----------------------3.27

'his equation is used in calculating the induced voltage in the loop antenna used for :ceiving radio signal. A model calculation is presented in Chapter VI.

References

[Beck48] G Bech. *Phys. Rev.* **74**, 795 (1948).

[Dooher71] John Dooher. *Phys.Rev. D,* **3**, 2652 (1971).

[Fermi40] E Fermi. *Phys.Rev.* **57**, 485 (1940).

[Garibian58] G M Garibian. *Soviet Phys. JETP* **6**, 1079 (1958).

[Garibian59] G M Garibian & G Chalikian. *Sov.Phys.JETP* **8**, 894 (1959).

[Ginzburg46] V L Gingburg & I M Frank. *Zh.Eksp.teoe.Fiz* **16** (1946).

[Ginzburg80] V L Ginzburg & V N Tsytovich. *Phys. Lett.* **79A**, 16 (1980).

[Pafomov58] V Pafomov. *Sov.Phys.JETP* **6**, 829 (1958).

[Saveliev02] V Saveliev. *Mathematical Modelling. RAS* **11**, 93 (2002).

CHAPTER IV

Loop Antenna

Loops are simple but fundamental forms of antennas. Most of the theoretical results available in the literature deal with the electrically small loop antennas which are of more interest because of their well accepted application in personal communication systems such as pagers and AM radio receivers. The term "small loop" is not exactly defined. Usually a loop with ka < 0.3 (where k, the wave number, is $2\pi/\lambda$ and a- is the radius of the loop) is considered to be small [Balanis05][Kraus01]. However most of the available theoretical results deal with much smaller antennas. In small loops, we can make the assumption of having a constant current around the loop, which makes it relatively easy to analyze. The main characteristic of the loop antenna which makes it interesting as a receiving antenna is the fact that loops have a dominantly magnetic near field and so the important parameter of the surrounding material would be the permeability instead of the permittivity. In this chapter some theoretical results on loop antennas are discussed and thereby the simulation results are examined about the best configuration of the loop for receiving purpose.

4.1 Small Loop Theory:

An electrically small loop (circular or square, etc.) is equivalent to an infinitesimal magnetic dipole whose axis is perpendicular to the plane of the loop with the following condition [Balanis05]

$$I_m l = j\pi a^2 \omega \mu I_0 \quad \text{---------------------4.1}$$

Where $I_m l$ is the magnetic moment of the dipole, a- is the loop radius and I- is the constant current on the loop. As the loop perimeter is assumed to be small compared to the wavelength, the changes in the sinusoidal current can be neglected and the current is considered constant. So, to find the radiation field and other parameters of the loop, one can follow the same procedure as for linear dipoles.

4.1.1 Radiation Field:

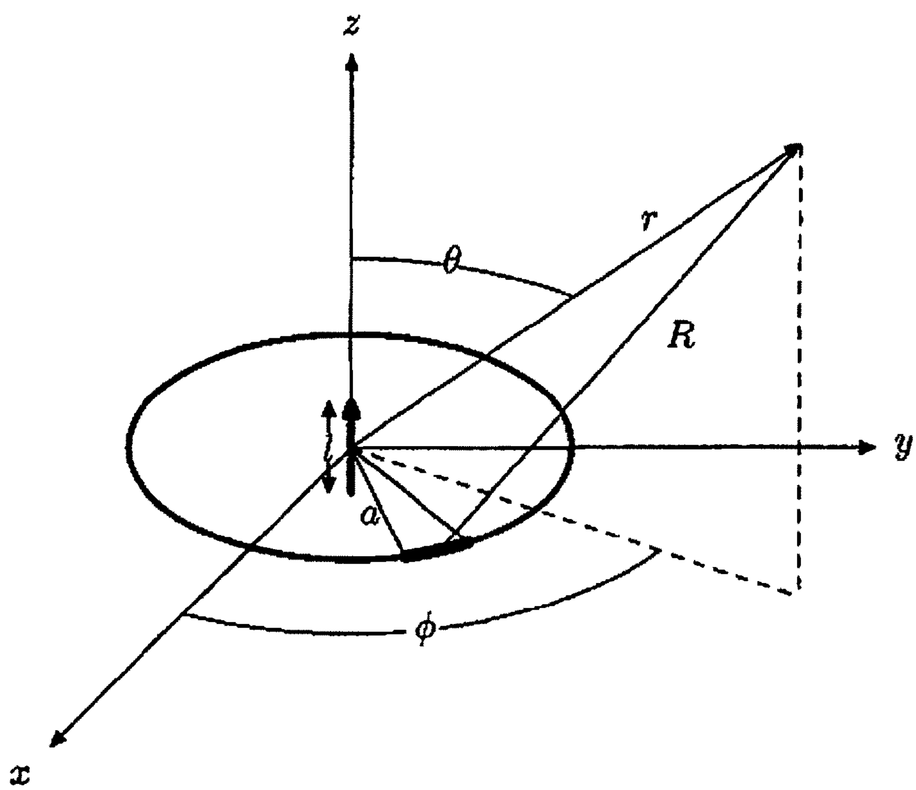

Figure 4.1 shows the geometry of the circular loop and magnetic dipole.

From [Balanis05], the radiation fields of a small loop (infinitesimal magnetic dipole) are

$$H_r = j\frac{ka^2 I_0 \cos\theta}{2r^2}\left[1+\frac{1}{jkr}\right]e^{-jkr} \qquad 4.2$$

$$H_\theta = -\frac{(ka)^2 I_0 \sin\theta}{4\pi}\left[1+\frac{1}{jkr}-\frac{1}{(kr)^2}\right]e^{-jkr} \qquad 4.3$$

$$H_\phi = 0 \qquad 4.4$$

Where I_o is the constant current on the loop. It can be seen that only the θ component of the H-field will survive to the far field.

When dealing with a magnetic dipole, we have a magnetic current density instead of an electric one. So we have M $\neq$ 0 (magnetic current density) and J = 0 (electric current density), and thus the corresponding electric field components are

$$E_r = E_\theta = 0 \quad \text{--} \; 4.5$$

$$E_\phi = \eta \frac{(ka)^2 I_0 \sin\theta}{4\pi}\left[1 + \frac{1}{jkr}\right]e^{-jkr} \quad \text{----------------------------} \; 4.6$$

where $\eta = \sqrt{\frac{\mu}{\varepsilon}}$ is the intrinsic impedance of the medium in which the radiation is taking place.

4.1.2 Power Density

The radiated power for an antenna can be calculated from integrating the power density over a closed sphere. The power density or the Poynting vector of an electromagnetic field is calculated as follows [Jackson98]

$$\mathbf{W} = \mathbf{E} \times \mathbf{H} \quad \text{--} \; 4.7$$

Where

$$E = \mathrm{Re}\left[E(x,y,z)e^{j\omega t}\right] \quad \text{--------------------------------------} \; 4.8$$

$$H = \mathrm{Re}\left[H(x,y,z)e^{j\omega t}\right] \quad \text{--------------------------------------} \; 4.9$$

E and **H** represent the instantaneous electric and magnetic field intensities respectively and E and H are the complex envelopes of the fields. So equation (4.7) can be written as

$$\begin{aligned}
W &= \mathrm{Re}\left[E(x,y,z)e^{j\omega t}\right] \times \mathrm{Re}\left[H(x,y,z)e^{j\omega t}\right] \\
&= \frac{1}{2}\left[Ee^{j\omega} + E^* e^{-j\omega}\right] \times \frac{1}{2}\left[He^{j\omega} + H^* e^{-j\omega}\right] \\
&= \frac{1}{4}\left[E \times H^* + E^* \times H\right] + \frac{1}{4}\left[E \times He^{2j\omega} + E^* \times H^* e^{-2j\omega}\right] \\
&= \frac{1}{2}\mathrm{Re}\left[E \times H^*\right] + \frac{1}{2}\left[E \times He^{2j\omega}\right] \quad \text{————————} \; 4.10
\end{aligned}$$

The first term of equation (4.10) is not a function of time but the second term is time dependent with twice the frequency of the fields. So the time average Poynting vector (average power density) will be

$$W_{av} = \frac{1}{2}\mathrm{Re}\left[E \times H^*\right] \quad \text{------------------------------------4.11}$$

The complex Poynting vector is defined as

$$W_{av} = \frac{1}{2}\left[E \times H^*\right] \quad \text{-- 4.12}$$

So the real part of the complex Poynting vector is the real radiated power density and the imaginary part presents the reactive stored power density. For the loop antenna we have

$$\begin{aligned} W &= \frac{1}{2}\left(E \times H^*\right) = \frac{1}{2}\left[\left(\hat{a}_\varphi E_\varphi\right) \times \left(\hat{a}_r H_r^* + \hat{a}_\theta H_\theta^*\right)\right] \\ &= \frac{1}{2}\left(-\hat{a}_r E_\varphi H_\theta^* + \hat{a}_\vartheta E_\varphi H_r^*\right) \\ &= \eta \frac{(ka)^4}{32}\left|I_0\right|^2 \frac{\sin^2\theta}{r^2}\left[1 + j\frac{1}{(kr)^3}\right]\hat{a}_r - j\frac{\eta k^2 a^3}{16}\left|I_0\right|^2 \frac{\sin 2\theta}{r^2}\left[1 + \frac{1}{(kr)^2}\right]\hat{a}_\theta \; Watt.m^{-2} \end{aligned}$$

$$\text{---------------------4.13}$$

After integrating over a closed sphere with radius r, because of the sin2θ factor in θ component, only the radial component contributes to the complex power P

$$W_r = \eta \frac{(ka)^4}{32}\left|I_0\right|^2 \frac{\sin^2\theta}{r^2}\left[1 + j\frac{1}{(kr)^3}\right] \quad Watt.m^{-2} \quad \text{---------------------- 4.14}$$

and so

$$P = \oint_S W.ds = \eta \frac{(ka)^4}{32}\left|I_0\right|^2 \int_0^{2\pi}\int_0^{\varphi}\left[1 + j\frac{1}{(kr)^3}\right]\sin^3\theta \, d\theta \, d\varphi \quad Watt \quad \text{---------- 4.15}$$

which reduces to

$$P = \eta\left(\frac{\pi}{12}\right)(ka)^4\left|I_0\right|^2\left[1 + j\frac{1}{(kr)^3}\right] \quad Watt \quad \text{----------------------- 4.16}$$

In the far field, the imaginary part of the power is negligible and we just have

$$P=\eta\left(\frac{\pi}{12}\right)(ka)^4|I_0|^2 \qquad Watt \text{ ---------------------- } 4.17$$

On the other hand, as can be seen in (4.8), when kr << 1 the imaginary part is dominant and the power is essentially reactive. The positive sign of the imaginary part of the power shows that the near field power is mainly inductive and the stored magnetic energy is larger than the electric energy.

4.1.3 Radiation Resistance and Ohmic Loss

Using the assumption of having a constant current around a small loop, the radiation resistance

of single loop antenna can be found from

$$P_{rad}=\frac{|I_0|^2 R_{rad}}{2} \qquad Watt \text{ ----------------- } 4.18$$

$$\Rightarrow R_{rad}=\eta\left(\frac{\pi}{6}\right)\left(k^2a^2\right)^2=20\pi^2\left(\frac{C}{\lambda}\right)^2 \qquad ohms \text{ ------ } 4.19$$

where $C = 2\pi a$ is the circumference of the loop and η is the impedance of the medium which in the case of free space is equal to 120π. If the loop antenna has N turns each being exposed to the same magnetic field, the radiation resistance is

$$R_{rad}=\eta\left(\frac{\pi}{6}\right)\left(k^2a^2\right)^2=20\pi^2\left(\frac{C}{\lambda}\right)^2 N^2 \qquad ohms \text{ -------------- } 4.20$$

Note that for this equation to hold, the total electrical length of the wire should be small enough to have the constant current still.

The ohmic losses are calculated directly from the losses in the wire loop. However in a multi turn loop, the spacing between the turns must be greater than five times the wire radius for this assumption to be met. Otherwise, the proximity effect of the turns must be

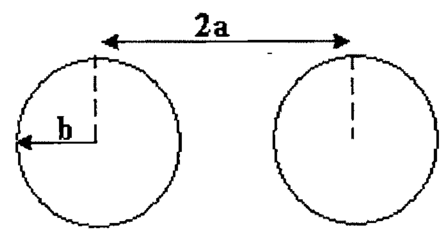

Figure 4.2 Cross section of the single loop

considered which will increase the ohmic loss. Considering this proximity effect [Smith72], the total ohmic resistance for an *N*-turn circular loop is given by

$$R_{ohmic} = \frac{Na}{b} R_s \left(\frac{R_p}{R_0} + 1 \right) \quad ohms \quad \text{------------------------} \; 4.21$$

Where

a = loop radius (m)

b = wire radius (m)

$R_s = \sqrt{\frac{\omega \mu_0}{2\sigma}}$ = surface impedance of the conductor (ohms)

R_p = ohmic resistance due to proximity effect (ohms)

$R_0 = \frac{NR_s}{2\pi b}$ = ohmic skin effect resistance per unit length (ohms/m)

Here we need the assumption of $\frac{a}{d_s}$ >> 1 where d_s is the skin depth and equal to $\left(\frac{2}{\omega \mu_0 \sigma} \right)^{1/2}$.

For the case of copper wire, the skin depth is around 2μm so we can easily assume that the condition is met.

4.1.4 Radiation Intensity and Directivity

The radiation intensity is defined as the radiated power per unit solid angle. This parameter is independent of distance and can be calculated from the power density, i.e.

$$U = r^2 W_{av} \qquad Watt.rad^{-2} \qquad \text{-------------------------} \; 4.22$$

The average power density, W_{av} of the antenna has only the radial component W_r from which we calculate the radiation intensity as

$$U = r^2 W_r = \frac{\eta}{2}\left(\frac{k^2 a^2}{4}\right)^2 |I_0|^2 \sin^2\theta = \frac{r^2}{2\eta}|E(r,\theta,\varphi)|^2 \qquad Watt.rad^{-2} \; \text{-----} \; 4.23$$

The pattern of the loop is identical to that of the infinitesimal dipole and the maximum value occurs at $\theta = \dfrac{\pi}{2}$ and is given by

$$U_{max} = \frac{\eta}{2}\left(\frac{k^2 a^2}{4}\right)^2 |I_0|^2 \quad Watt.rad^{-2} \qquad \text{------------------------} \; 4.24$$

The radiation intensity averaged over the sphere is given by

$$U_{av} = \frac{P_{rad}}{4\pi} \quad Watt.rad^{-2} \qquad \text{------------------------------------} \; 4.25$$

The directivity of an antenna is a parameter which relates only to the radiation pattern. It shows the ratio of the power radiated in a specific direction to the total radiated power. So the directivity of the loop can be found as

$$D_0 = 4\pi \frac{U_{max}}{P_{rad}} = \frac{3}{2} \qquad \text{---------------------------------} \; 4.26$$

4.1.5 Efficiency

The antenna efficiency is defined as $\dfrac{R_{rad}}{R_{rad} + R_{ohmic}}$. As radiation resistance of a small loop antenna is so small compared to its ohmic resistance, the antenna efficiency is normally low. However the efficiency can be increased using two different methods----

1. Using multi-turns antennas: For loops with N turns, R_{rad} in creases in proportion to N^2 while R_{ohmic} in creases in proportion to N. So increasing the number of turns will improve the efficiency.

2. Placing a high permeability core made of ferrite material in the wire loop: Using this method, the magnetic flux passing through the loop increases. With ferrite relative permeability $\mu_{rf} = \frac{\mu_f}{\mu_0}$ occupying the core of the loop, the antenna can be analyzed according to the relative effective permeability $\mu_{cr} = \frac{\mu_e}{\mu_0}$ and thus the radiation resistance is

$$R_{rad} = 20\pi^2 \left(\frac{c}{\lambda}\right)^2 N^2 \mu_{er}^{\ 2} \qquad ohms \qquad \text{--------------------} \ 4.27$$

The effective permeability has been measured by Wolf (1966) for a cylindrical ferrite core as follows [Vaughan03],[Wolf66]

$$\mu_e = \frac{\mu_f}{1 + D_\mu(\mu_f - 1)} \approx \frac{1}{D_\mu} \qquad H.m^{-1} \qquad \text{--------------------} \ 4.28$$

where the empirical demagnetization factor is given by $D \approx e^{-(1.54\log(LOD)+0.52)}$ and LOD is the length over diameter of the ferrite core. The formula is held for LODs between about 3 and 100.

4.2 Multi-turn loops

One of the main solutions to increase the efficiency through increasing the impedance of the loop antenna is using multi-turn loops. For loops with N turns, R_{rad} increases in proportion to N^2 while R_{ohmic} increases in proportion to N. So increasing the number of turns will improve the efficiency. Usually, $R_{ohmic}$is directly calculated from the wire losses. However in a multi-turn loop, the spacing between the turns must be greater than five times the wire radius for this assumption to be met [Smith72]. Other wise, the proximity effect of the turns must be considered which will increase the ohmic loss.

4.2.1 Proximity Effect

As mentioned before, considering the proximity effect, the total ohmic resistance for an N-turn circular loop is given by

$$R_{ohmic} = \frac{Na}{b} R_s \left(\frac{R_p}{R_0} + 1 \right) \quad \text{--------------------} \; 4.29$$

The fact is that when two current conducting wires are placed next to each other, the current distribution in each of them will be affected by the fields of the other one. This effect will increase the ohmic resistance. Figure 4.3 shows this effect on the surface current of two wires next to each other in comparison to a single wire. Figure 4.4 shows the cross section of multiturn loop and 4.5 shows the amount of added resistance due to proximity effect [Smith72]

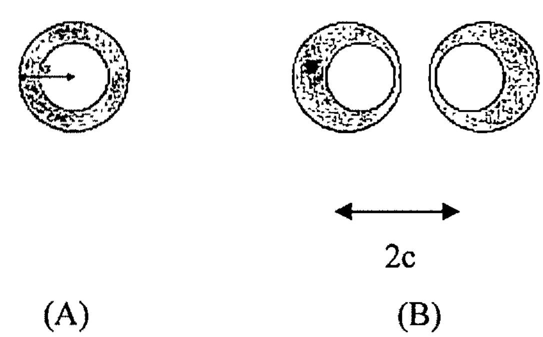

Figure 4.3: The effect of placing two wires next to each other, on their surface current distributions. The thickness of the shadowed area shows the distribution of current on the surface of the wire.

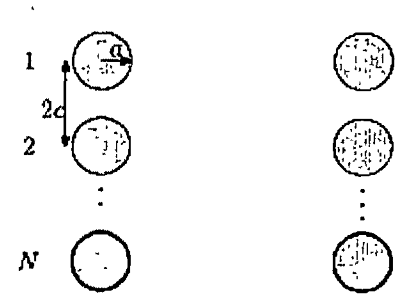

Figure 4.4: N-turn loop (2c is the spacing between the turns)

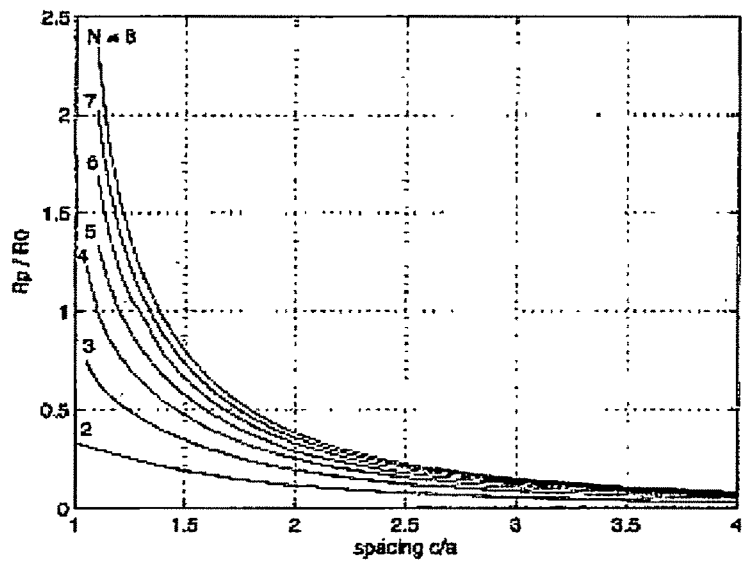

Figure 4.5: Additional ohmic resistance per unit length of a loop having N-turns [Vaughan03[[Smith72]

4.3 Receiving Loop antenna:

The aim of any receiving antenna is to convert an electromagnetic wave into a voltage. A magnetic loop antenna is a winding of copper wire around a frame or around ferromagnetic material.

A loop antenna is actually sensitive to the magnetic field and not the electric field. It outputs a voltage proportional to that field. A particularity of this type of antenna is to provide a voltage proportional to the frequency of the signal. The antenna performance is influenced by the number of turns and the area of each loop. For a ferrite antenna, the permeability of the core increases the output voltage.

LF/VLF receiving loop antennas are very small electrically. The current in the loop is relatively uniform because of the small capacitance between the windings and to the shield.

ıder theses simplified conditions the induced voltage in a small air core loop antenna or the ltage appearing between the terminals of the antenna is given by [Straw07]

$$V= 2\pi\mu_0 NfAH\cos\theta \text{ -------------------------- } 4.30$$

$$V= 2\pi\sqrt{\mu_0\varepsilon_0}\ NfAE\cos\theta \text{ ---------------------- } 4.31$$

here μ_0 is the permeability of free space, ε_0 is the permittivity of free space N is the mber of turns, f is the frequency of the signal, H is the magnetic field intensity of the :ident radio signal, E is the electric field intensity of the incident radio signal and θ is the gle the flux lines make with the loop axis.

4 – Simulation with LTspice IV:

For an electrically small loop (circumference$\leq\lambda/10$) antenna, the circumference termines the efficiency of the antenna. The far fields of such antennas are dependent on the ›p area but are independent of the loop shape. Since the magnetic vector potential

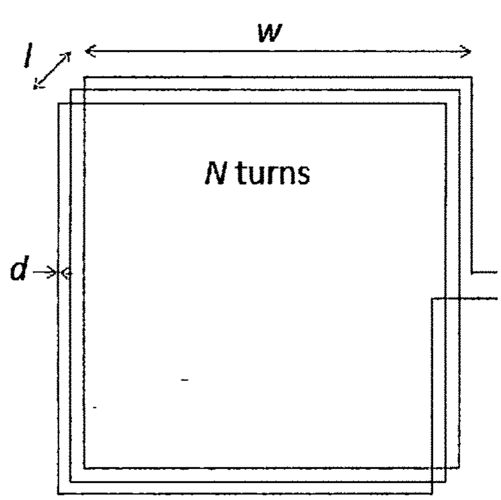

Figure 4.6 A typical square loop antenna

egrations required for a circular loop are more complex than those for a square loop, the ıare loop is considered in the derivation of the characteristics an electrically small loop antenna [Straw 07]) of any shape with same electrical size. We therefore consider a square loop antenna for simulation purpose. A typical square loop is shown in the figure 4.6 where

- w is the frame side length, Total wire length $4Nw$.
- d is the wire diameter, Wire perimeter is πd.
- l is the length of the winding,

The response of the receiver (loop antenna) has been simulated using LTspiceIV. The sequence of the simulation is as follows.

1. Design of equivalent electrical circuit of loop antenna
2. Define the parameters
3. Design of the spice model of loop antenna.
4. Simulation

4.4.1 Electrical Equivalent Circuit

The electrical equivalent circuit of loop antenna is shown in figure 4.7 with the following circuit components-

i) an ideal voltage generator V with a value given by the equation 3.30

ii) the radiation resistance R_{rad} defined by the equation—

iii)the loop induction L_{loop}

iv) the wire inductance L_{wire}

v) the wire resistance R_{dc}

vi) the skin effect and proximity effect resistance R_{ac}

vii) the distributed capacitance C_{loop}

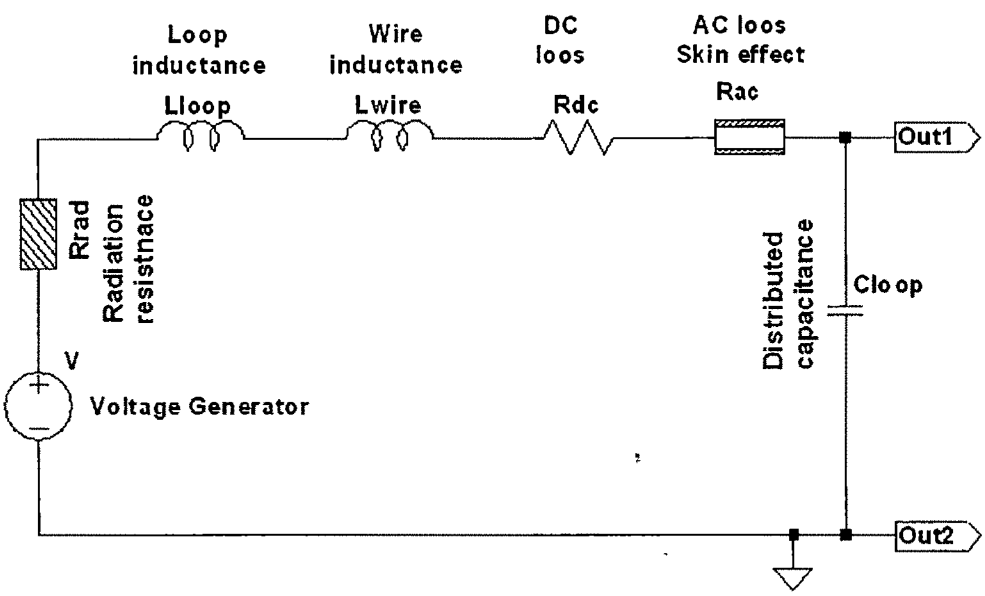

Figure 4.7 Equivalent electric circuit of a loop antenna.

4.4.2 Model Parameters:

4.4.2.1 Radiation Resistance (R_{rad})

The radiation resistance which is a virtual resistance gives the measure of the amount of losses in the antenna during the transformation of electromagnetic energy into electric energy. From equation 4.20 we have

$$R_{rad} = 20\pi^2\left(\frac{C}{\lambda}\right)^2 N^2 \qquad ohms$$

After simplifying we get

$$R_{rad} = Z_0 \frac{8}{3}\pi^3\left(\frac{NA}{\lambda^2}\right)^2 \text{--------------------}4.33$$

where

- R_{rad} is the radiation resistance, in Ω
- Z_0 is the impedance of free space
- C is the circumference of the loop

- N is the number of turns
- A is the area of each winding, in m²
- λ is the wavelength, in m

4.4.2.2 Loop Inductance L_{loop}:

It gives the measure of the total inductance of the wire windings around the frame and defined by the equation for a square frame of air core loop [Straw07]

$$L_{loop} \approx 8\times10^{-7} N^2 w\left(\ln\left(\frac{1.4142wN}{(N+1)l}\right)+0.37942+\frac{0.3333(N+1)l}{wN}\right) \quad \text{----------4.34}$$

where:

- L_{loop} is the wiring inductance, in H
- N is the number of turns
- w is the frame side length, in m
- l is the length of the winding, in m

4.4.2.3 Wire inductance L_{wire}

The wire of the antenna windings has itself an inductance. A wire of length $4Nw$ has an inductance L_{wire} according to [Wilson08]

$$L_{wire} \approx \frac{\mu_0\,(4Nw)}{2\pi}\cdot\left(2.303\log\left(\frac{4.(4Nw)}{d}\right)-1+\frac{\mu_r}{4}+\left(\frac{d}{2\cdot(4Nw)}\right)\right)$$

$$\approx 2\cdot10^{-7}\cdot(4Nw)\cdot\left(2.303\log\left(\frac{16Nw}{d}\right)-0.75+\left(\frac{d}{8Nw}\right)\right) \quad \text{-------------------4.35}$$

where:

- L_{wire} is the wire inductance, in H.
- N is the number of turns
- w is the frame side length, in m. Total wire length is $4Nw$.
- d is the wire diameter, in m.

4.4.2.4 Wire resistance R_{dc}

Electric wire has a resistance that is function of its length and diameter. The resistance of a wire of length $4Nw$ and of diameter d is determined by:

$$R_{dc} = \frac{(4Nw)\cdot\rho}{\pi d^2 / 4} \quad \text{----------------------4.36}$$

where:

- R_{dc} is the wire resistance, in Ω
- N is the number of turns
- w is the frame side length, in m. Total wire length is $4Nw$.
- d is the wire diameter, in m. Wire cross section is $\pi d^2/4$.
- ρ is the copper resistivity, in Ω·m. ρ=16.78nΩ·m.

This resistance is a source of thermal white noise according to the Johnson-Nyquist formula that expresses the voltage spectral density of the thermal noise by:

$$\overline{V}_{noise} = \sqrt{4kTR} \quad V/\sqrt{Hz}$$

k is the Boltzmann constant ($1.38\cdot 10^{-23}$ J/K), T is the absolute temperature in kelvins, and R is the resistance in ohms.

4.4.2.5 Skin effect and proximity effect resistance R_{ac}

The skin effect resistance is [smith72]:

$$R_{ac} = \frac{4Nw}{\pi d}\sqrt{\pi \mu_0 f \rho} \quad \text{----------------------------------4.37}$$

where:

- R_{ac} is the skin effect resistance, in Ω
- N is the number of turns
- w is the frame side length, in m. Total wire length $4Nw$.

- d is the wire diameter, in m. Wire perimeter is πd.
- μ_0 is the permeability of free space ($4\pi 10^{-7}$ H/m)
- f is the frequency, in Hz
- ρ is the copper resistivity, in $\Omega\cdot$m. ρ=16.78n$\Omega\cdot$m.

4.4.2.6 Distributed capacitance C_{loop}

The distributed capacitance approximately equals to [Wilson08]

$$C_{loop} \approx 3.9685 \cdot 10^{-13} \cdot \sqrt[3]{\frac{\left(400w/\pi\right)^4}{100l}} \quad 4.38$$

where:

- C_{loop} is the distributed capacitance of a square frame, in F
- w is the frame side length, in m
- l is the winding length, in m

This formula is also valid for ferrite antennas, by replacing w by the diameter of the windings.

4.4.2.7 Spice model of Loop antenna

Figure 4.8 shows the schematic diagram of spice model of loop antenna. The ideal voltage generator B_{loop} implements equation (4.30). A Laplace transform is used to model the frequency dependency of the voltage. V_{field} is a voltage generator that emulates an electric field of 150μV/m. The schematics implement the various elements of the antenna electric model and the associated equations.

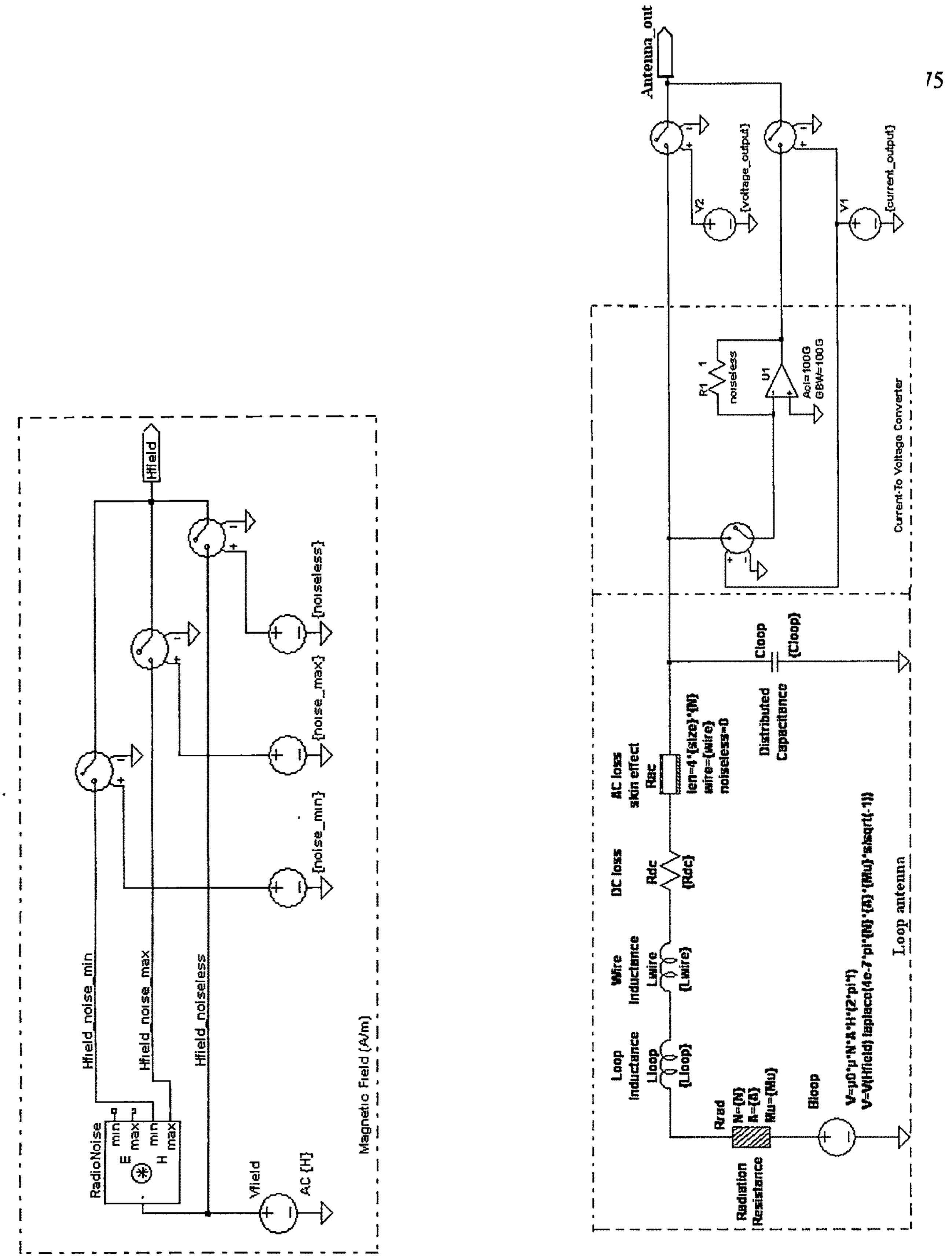

Figure 4.8 Spice Model of Loop antenna

4.4 Results

4.4.1 AC analysis

In AC analysis, simulation has been done for antenna out put voltage and antenna out put current. An electric field of 150μV/m has been generated and converted to its equivalent magnetic filed. The magnetic field is fed to the input of the antenna as the incident magnetic field. Figure 4.9 shows the simulation results of output voltage and figure 4.10 shows the output current in the antenna load:

It has been found that in the open circuit plot i.e Rload=100MegΩ, we have a linear response with a rising slope of 20dB per decade corresponding to the evolution with the frequency of B_{loop}. From about 100 kHz, the circuit starts to resonate which is shown by the peak in the figure 4.9.

For short circuit plot the output voltage became constant beyond 1kHz frequency. The same response is also observed for 50Ω load resistance.

From figure 4.10 we have seen that with a closed circuit, the frequency response is flat. The distributed capacitance has no detrimental effect since it is shorted. By using an operational amplifier as a current-to-voltage converter; it is possible to have almost null impedance at the antenna output. In this specific case, a transresistance of 100kΩ will give a linear response in the whole VLF band.

By using non-null impedance, the antenna linearity is reduced, and has finally a resonant behavior such as the one observed with the voltage measurements as shown in figure 4.10.

Thus we have seen that if the antenna is intended to be used over a wide band, it is necessary to connect it to short impedance and to work with its current. An operational amplifier can be used as a current-to-voltage converter. The linearity is then only limited in the low frequencies by the antenna resistance.

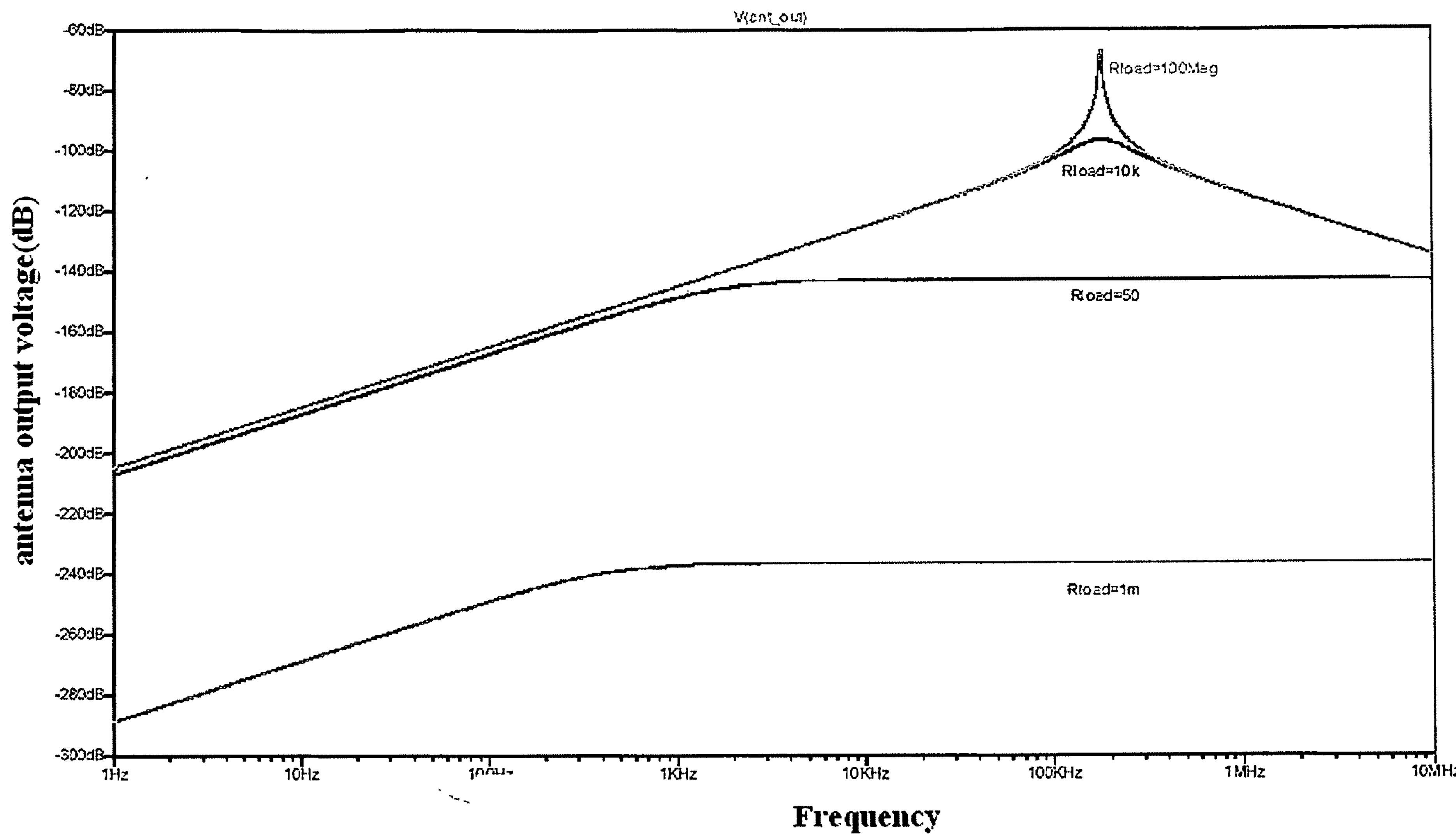

Figure 4.9 Spice simulated results of antenna output voltage in the frequency ragne of 1Hz-10MHz.

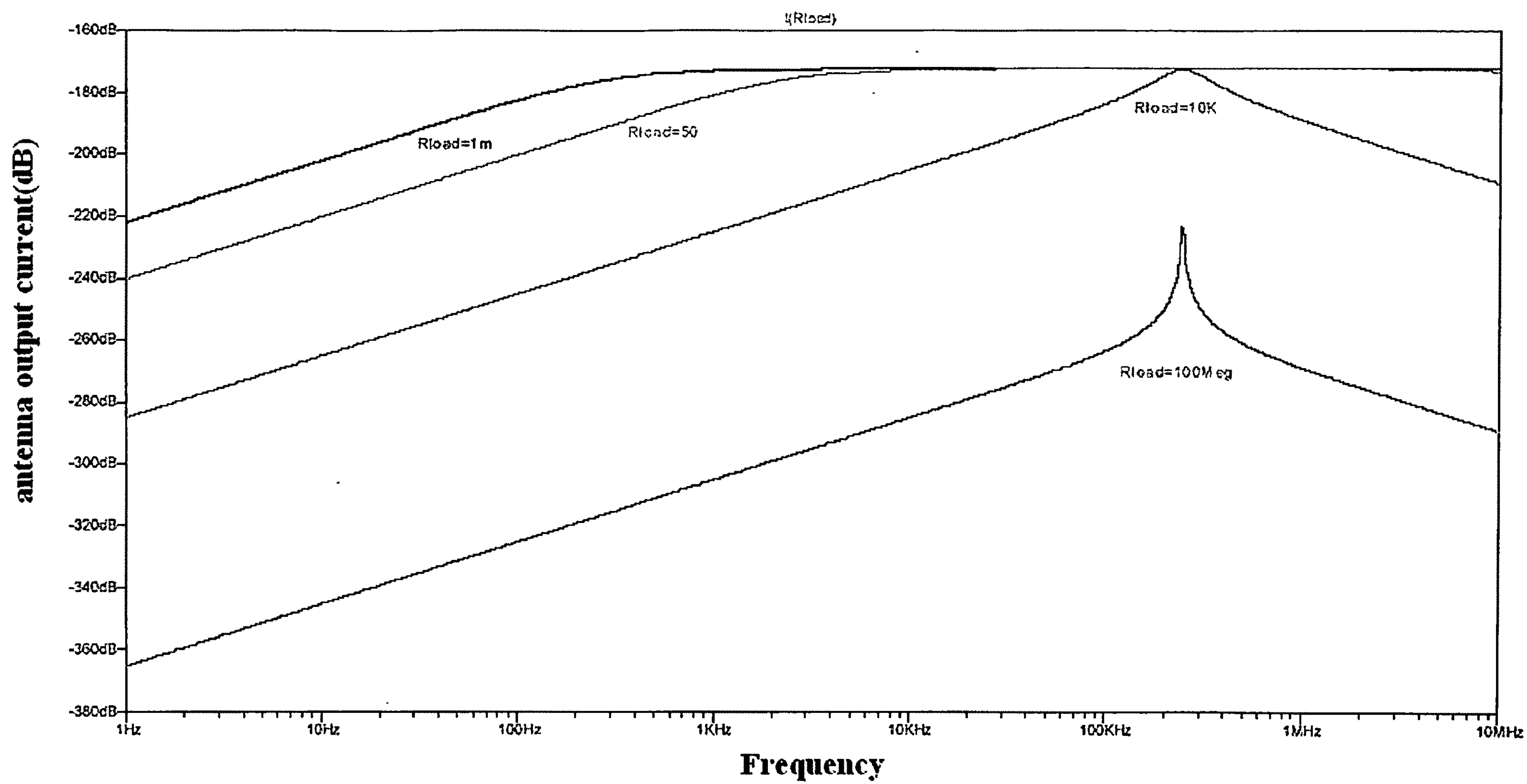

Figure 4.10 Spice simulated results of antenna output current in the frequency ragne of 1Hz-10MHz.

ł.4.2 Noise analysis

A model of electric and magnetic fields noise spectral density has used Loudnet10] for noise analysis of the receiver with the following three different noise evels-

i) antenna noise with zero atmospheric noise
ii) antenna noise with minimum atmospheric noise
iii) antenna noise with maximum atmospheric noise

Atmospheric noise sources are man-made noises and galactic noises between).1Hz and 100MHz. Minimum and Maximum noise expected values are defined by ITU-ł P.372-8. Figure 4.11 shows the results of the noise voltage at the antenna output.

Figure 4.12 shows the noise voltage at the antenna output when antenna is vorking in current mode. The current plots show the current noise spectral density, in \/√Hz Those values are obtained by adding at the output of the antenna an ideal ›perational amplifier acting as a current-to-voltage converter with a noiseless ransresistance of 1Ω. The noise voltage spectral density calculated by SPICE at the ›utput of the converter reflects the current noise spectral density at the shorted outputs of he antenna. Table 4.1 gives the values of integrated noise voltage and Table 4.2 gives 'alues of integrated noise current of the receiving antenna at different bandwidth.

Table 4.1 Values of integrated noise voltage of the receiving antenna

Bandwidth	RMS noise voltage		
	Antenna only	Antenna & minimum noise	Antenna & maximum noise
1Hz-10MHz	12.09 μV	27.43 μV	13.73 mV
10kHz-100kHz	133.77 nV	830.6 nV	132.74 μV
29.8kHz-34.2kHz	8.08 nV	41.45 nV	6.75 μV

Table 4.2 Values of integrated noise current of the receiving antenna.

Bandwidth	RMS noise current		
	Antenna only	Antenna & minimum noise	Antenna & maximum noise
1Hz-10MHz	1.06 nA	3.8 nA	154.1 nA
10kHz-100kHz	159 pA	2.59 nA	123 nA
29.8kHz-34.2kHz	11.4 pV	58.4 pV	9.5 nA

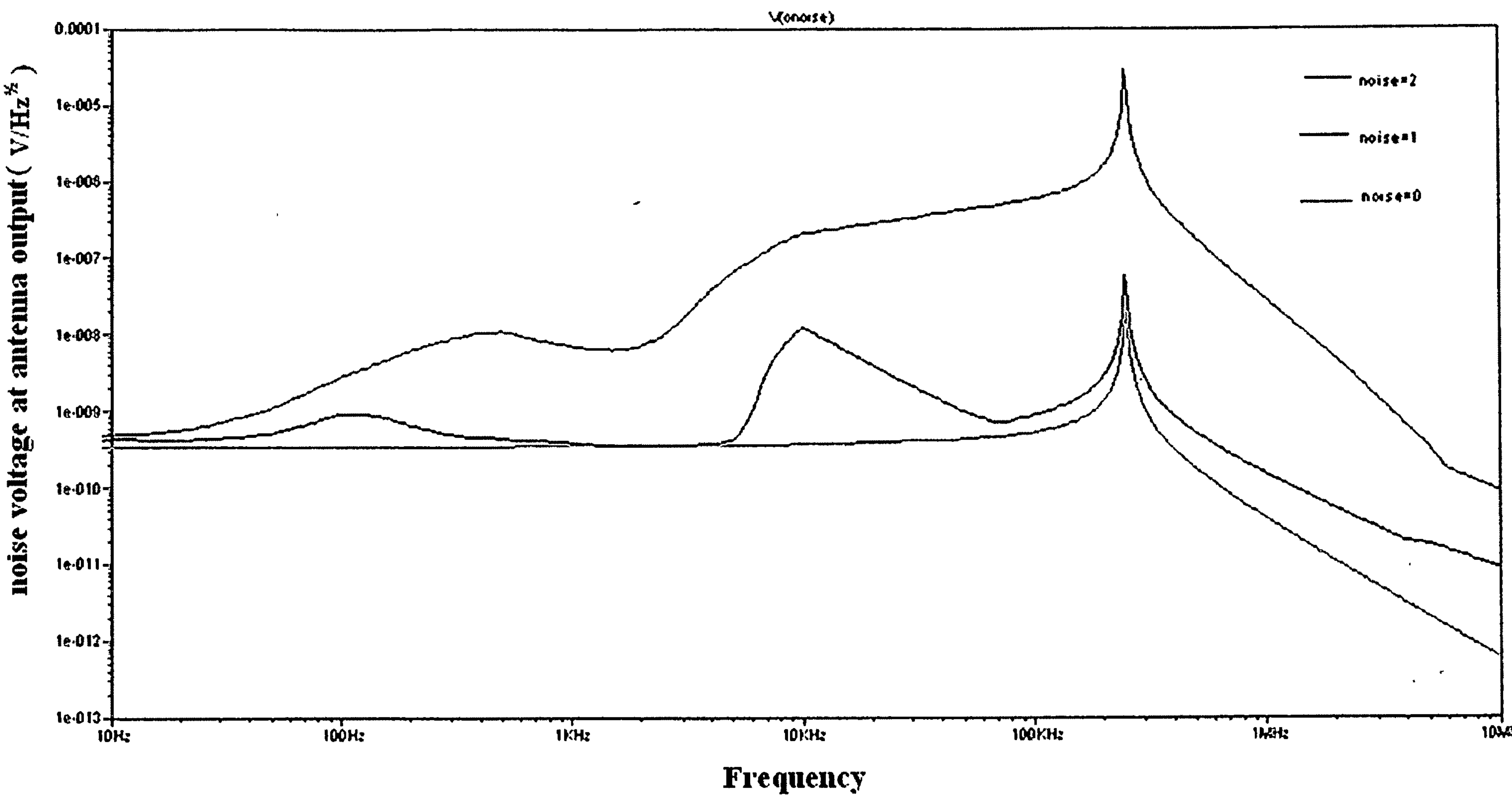

Figure 4.11 Spice simulated results of antenna output noise voltage in the frequency range of 1Hz-10MHz.

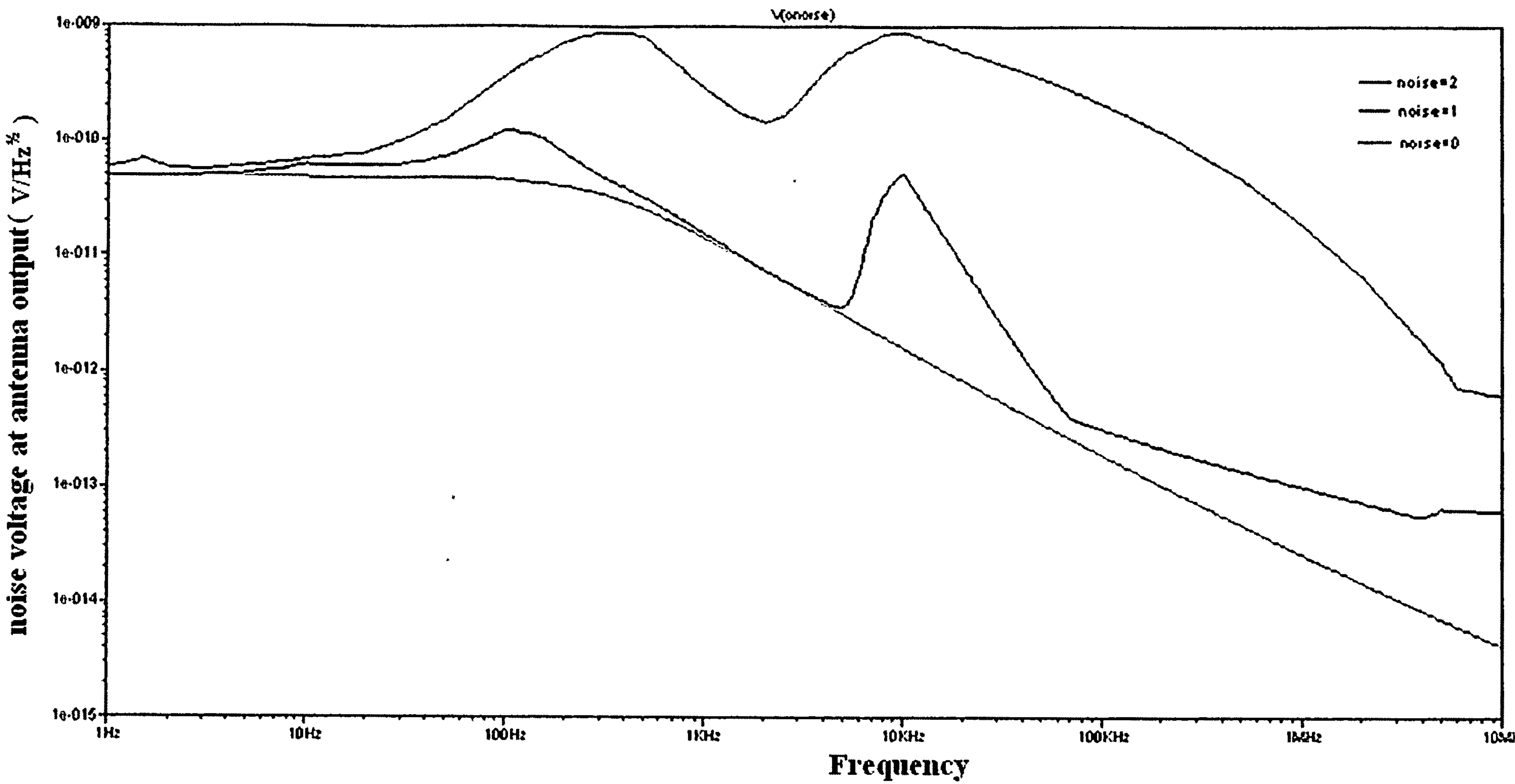

Figure 4.12 Spice simulated results of antenna output noise voltage in the frequency range of 1Hz-10MHz, when antenna is working in current mode.

4.4.3 Signal to Noise Ratio (SNR)

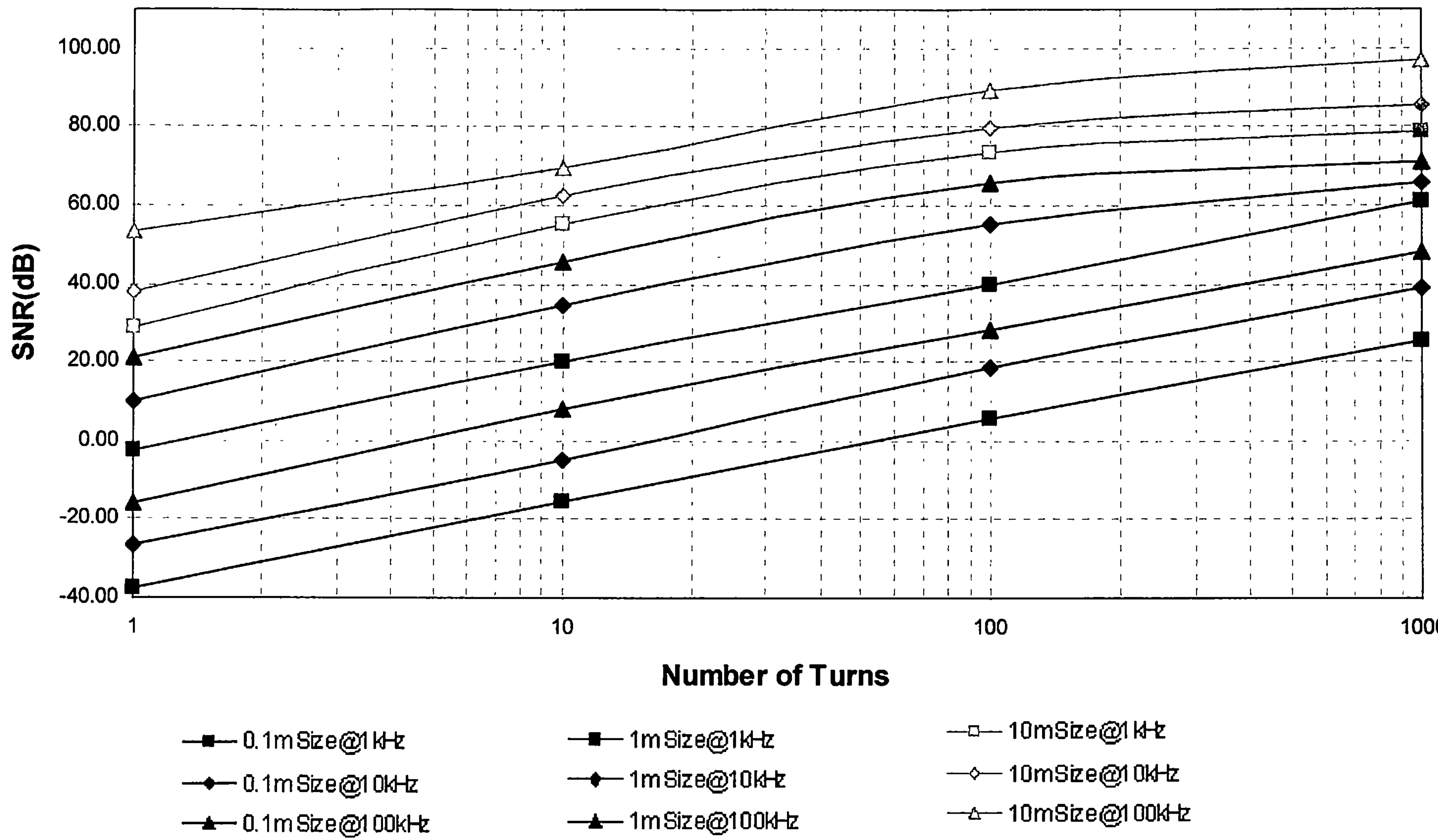

Figure 4.13 Spice simulated results of SNR of the receiving antenna with zero atmospheric noise.

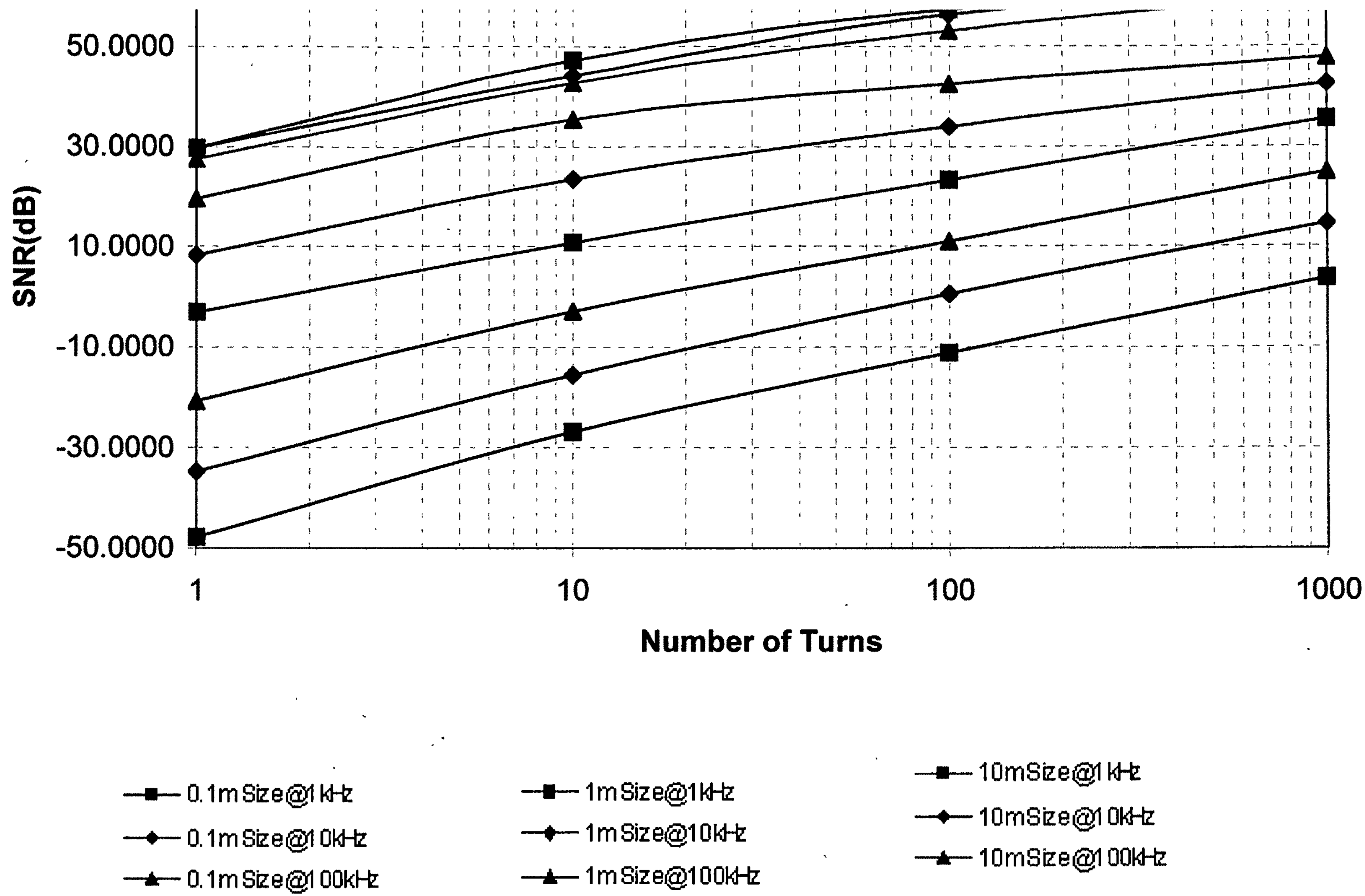

Figure 4.14 Spice simulated results of SNR of the receiving antenna with minimum atmospheric noise

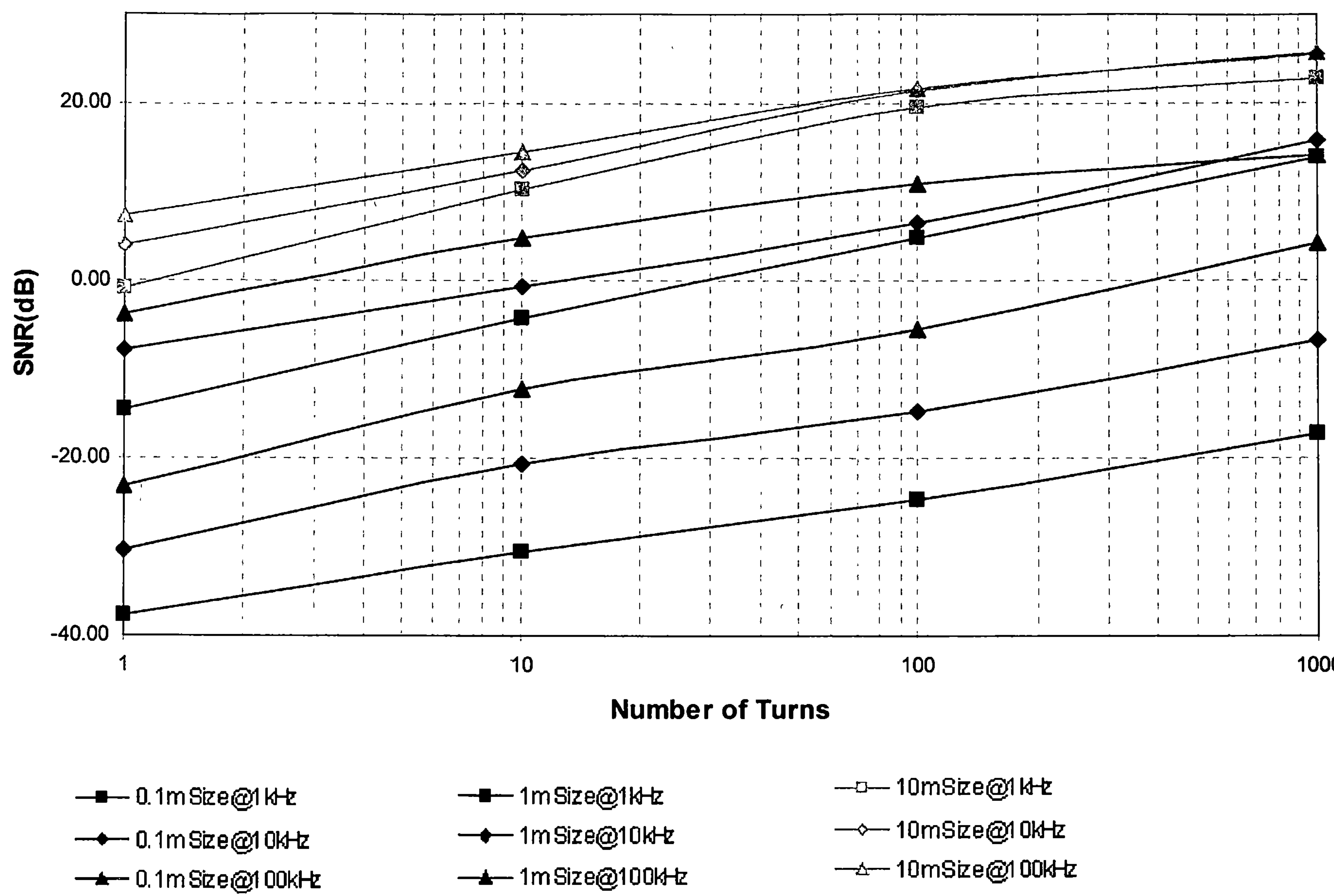

Figure 4.15 Spice simulated results of SNR of the receiving antenna with maximum atmospheric noise

SNR values have been determined by SPICE simulations of square loop antennas. The model used here corresponds to a untuned antenna working in current mode.

Plots SNR against the number of turns for antenna sizes of 0.1m by 0.1m, 1m by 1m and 10m by 10m are shown in figures 4.13-4.15.

For each antenna size, the SNR values have been determined around the frequencies of 1 kHz, 10 kHz and 100 kHz. The calculations have been made for a electric field of 150 μV/m at the antenna, which is a reasonably moderate signal level.

Figure 4.13 shows the SNR with no radio noise situation. This is a theoretical and ideal situation, where the noise figure is only influenced by the antenna noise. In this case, one can clearly see the influence of the antenna dimensions on the SNR ratio where SNR increases with increase in antenna dimension as well as increase in number of turns.

Figure 4.13 shows the SNR with no radio noise situation which is the actual condition. Here we see that the antenna efficiency with respect to SNR gets non linear with respect to size or number or turns. For a "big" antenna (10m side), the number of turns has no effect at all, so a single turn antenna is sufficient, for all frequencies of interest. For an antenna with a side of 1m, the influence of the number of turns gets marginal above a few tens of turns.

Figure 4.15 corresponds to worst case conditions of radio noise. In this case, the influence of the antenna characteristics on its overall capability to extract useful signal from the overwhelming noise is quite limited.

References

[Balanis05] Constantine A Balanis. *Antenna Theory* (Wiley-Interscience, 2005).

[Jackson98] J D Jackson. *Classical Electrodyanics* (John Wiley and Sons, New York, 1998).

[Kraus01] J D Kraus & R J Marhefka. *Antennas* (McGraw-Hill Education Singapore, 2001).

[Loudnet10] Lionel Loudnet,http://sidstation.lionelloudet.homedns.org/. in .(2010).

[Smith72] G S Smith. Proximity effect in system of parallel conductors. *Applied Phsics* **43** (1972).

[Straw07] R Dean Straw (ed.) *The ARRL Antenna Book* (2007).

[Vaughan03] R G Vaughan & J B Anderson. *Channels, Propagation and Aantennas for Mobile Communications* (The Institute of Electrical Engineers, London, UK, 2003).

[Wilson08] Mark J Wilson & Steven R Ford (eds.) *ARRL Hand Book of Radio Communication* (2008).

[Wolf66] E A Wolff. *Antenna Analysis* (Wiley, 1966).

CHAPTER V

Testing, Calibration and Experimental setup

A receiving antenna is a device which, when placed in an electromagnetic field, permits the extraction of energy from the field. It is possible to measure the field strength of electric or magnetic field components of an incident electromagnetic wave, only by means of suitably tested and calibrated antenna. At VLF, there are two types of receiving antennas or sensors: (1) E field sensors which are usually vertical monopoles and (2) H field sensors which are usually either air core or magnetic core loops.

In general, receiving antennas have the same basic properties as transmitting antennas. The size normally encountered, however, is different; VLF transmitting antennas are usually quite large physical structures whereas the receiving antennas are generally much smaller.

To detect the UHECRs an array of eight plastic scintillation detectors is setup inside a hut at the rooftop of physics building covering a total carpet area $2m^2$. Each particle detector consists of a scintillation block of size $50 \times 50 \times 5$ cm^3, a photomultiplier tube (PMT) EMI 9807B, a photomultiplier base, a preamplifier unit and a light tight enclosure. Figure5.1 shows a schematic view of a particle detector of miniarray. The PMT's are light sensitive detectors which provide a current output proportional to the intensity of incident light. During the passage of a charged particle through the scintillators, internal state of atoms are disrupted and light is emitted usually in a kind of domain effect yielding a pulse of light . The emitted light from the scintillation block falls on the photocathode of PMT and produces secondary electrons. These secondary electrons are electrostatically accelerated and focused into the dynode. Each dynode produces a number of secondary electron which are in turn accelerated and focused into the next dynode. The process is repeated at each subsequent dynode and secondary electrons from the last dynode are colleted at the anode. The anode signal is further processed by the preamplifier attached with the PMT base before sending to the control room for further processing and recording. Necessary low voltage for operation of the preamplifier and high voltage for the PMT dynode chain is supplied to the unit through their respective terminals

In this chapter we discuss the testing, calibration of radio receiving channels and particle detectors followed by the discussion of the experimental setup.

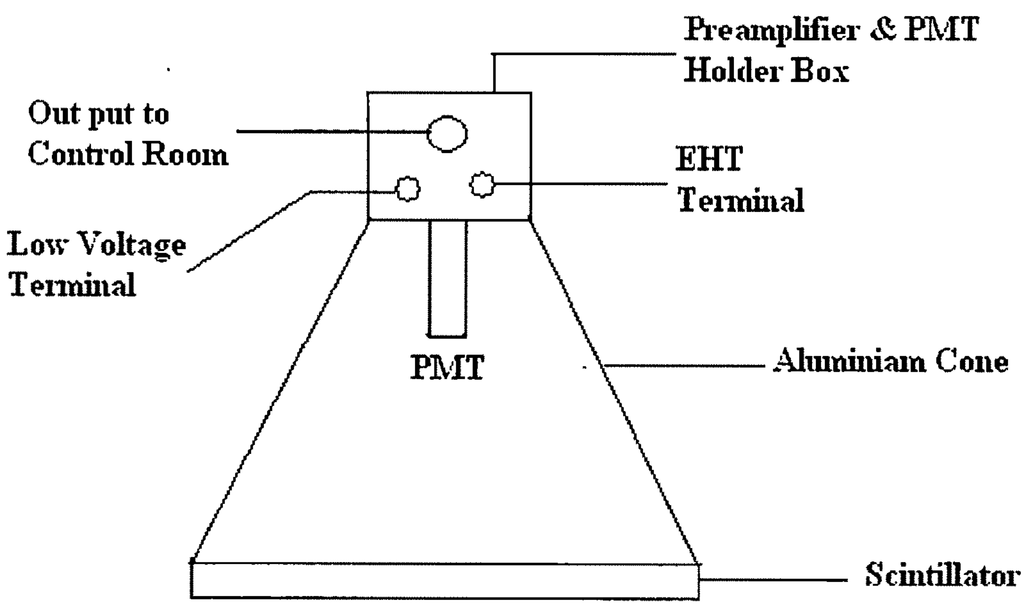

Figure 5.1 Schematic view of a Particle detector of miniarray hut

5.1 Loop antenna

Due to construction as well as installation simplicity we chose air core loop antenna to receive the magnetic components of the radio signal associated with UHECRs. These antennas were designed based on the simulation results on LTspice which is discussed in the chapter III.

Table: 5.1 Receiving Loop antenna parameters.

Number of turns	40
Total length of the wire	105600mm
Diameter of the wire	0.723 mm
[winding pitch]/[wire diameter]	1.5
Width of the winding	28.92mm
Diameter of the Loop	750mm
Self resonant frequency	700kHz

5.1.2 Testing

The radio signal receiving channel is tested initially with the help of local radio station. All India Radio (AIR) of Guwahati broadcasts using 755 kHz and 1.08 MHz frequency in the short wave band. The loop antenna is kept on the roof of Physics Building without preamplifier and low pass filter. Received signal is monitored with DSO [Tektronix TDS 2200] and stored in PC via GPIB interface. Figure5.3 shows the received signal and figure 5.3 shows the FFT of received radio signal.

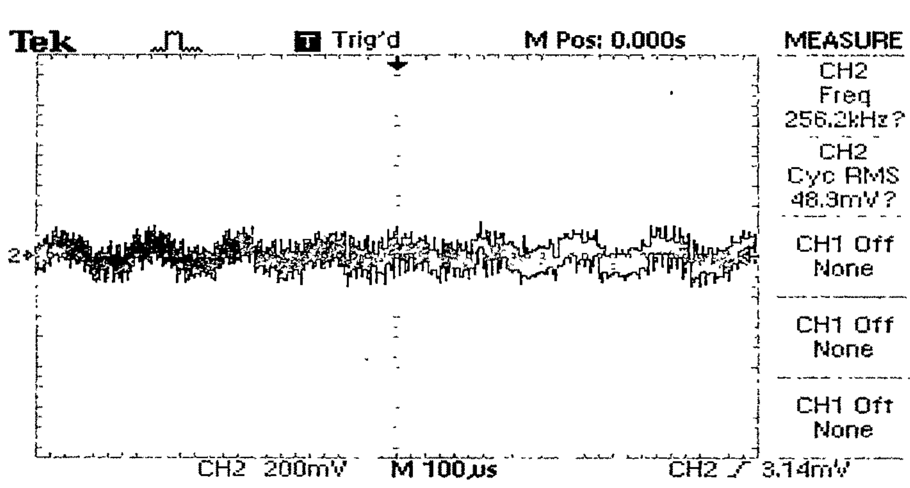

Figure 5.3 Received radio signal when antenna was installed in the rooftop of Physics building without preamplifier and band pass filter.

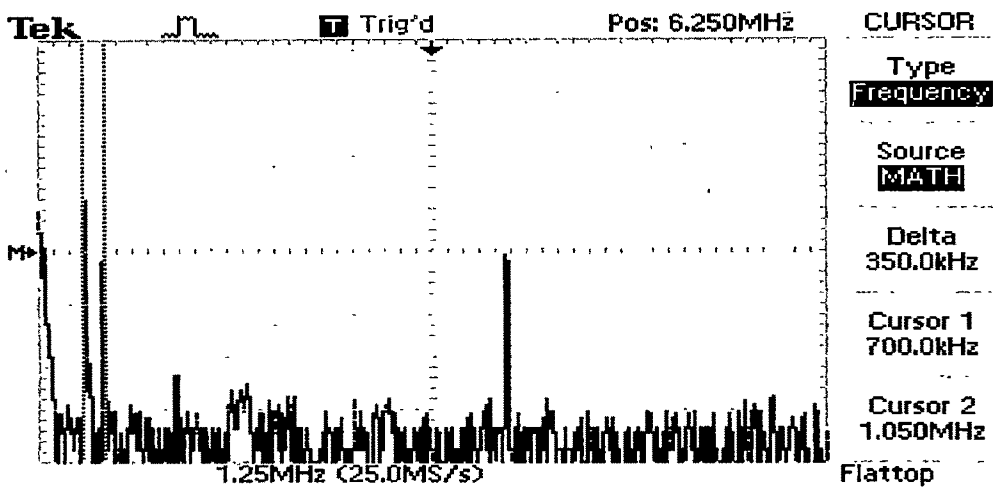

Figure 5.4 FFT of received radio signal when the antenna was installed in the rooftop of Physics building without preamplifier and band pass filter.

5.1.3 Calibration

Standard field method is used to calibrate the receiving loop antennas [Jean61]. A single turn, unshielded, balanced Loop antenna is used to produce the standard field in the calibration site. Power lines and metallic objects are cleared to avoid any influence or distortion of the calibration field in the calibration site. The calibration of the entire system, including Pre-amplifier, Low pass filter and receiving loop antenna is performed by placing the receiving antenna in a known field produced by the transmitting antenna, generated in the calibration room. The magnitude of the field at the receiving loop, produced by the single turn circular transmitting loop, is given by the equation 5.1 [Jean61]

$$H = \frac{r_1^{\,2} I}{2(d^2 + r_1^{\,2} + r_2^{\,2})^{3/2}} \sqrt{1 + \left(\frac{2\pi d}{\lambda}\right)^2}$$

(5.1)

where H- is the magnetic field strength in rms amperes per meter, r_1- is the radius of the transmitting loop in meters, r_2-is the radius of the receiving loop antenna, d- is the axial spacing in meters between the two co-axial loops , I- is the transmitting loop current in rms amperes and λ -is the free-space wave length in meters.

Equation 5.1 is valid for determining the magnetic field strength only when r_1, r_2 and d are small compared to wave length (λ). The loop spacing should be at least four times the radius of the larger of r_1 and r_2 for equation 5.1 to be valid within one percent [Jean61]

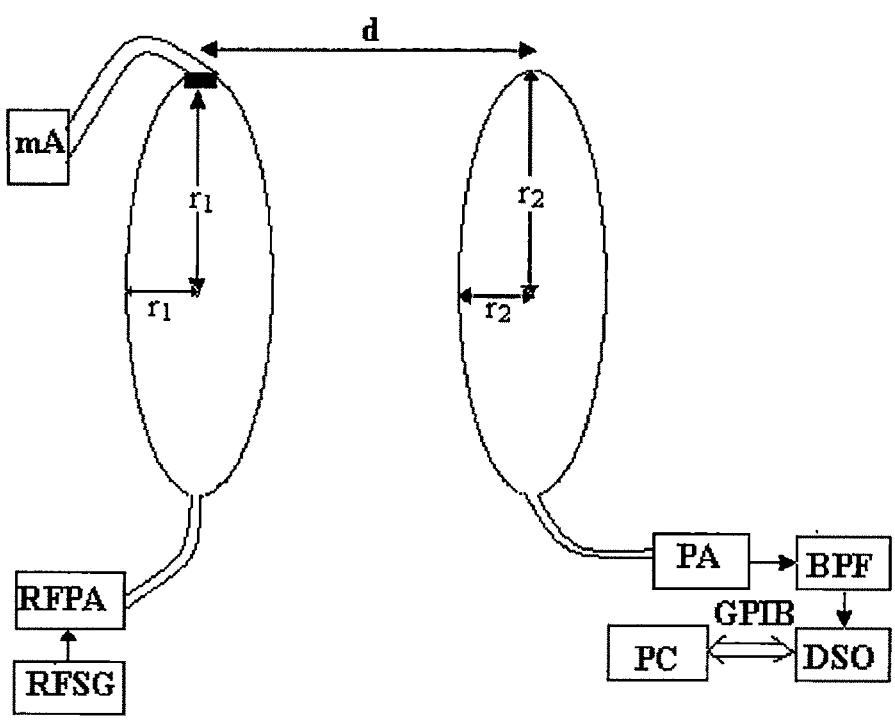

RFPA-Radio frequency Power Amplifier, RFSG- Radio Frequency Signal Generator, PA- Preamplifier, BPF-Band Pass Filter, DSO- Digital Storage Oscilloscope, PC-Personal Computer

Figure 5.5 Experimental arrangement for Calibration of receiving loop

The arrangement is shown in figure 5.5. The transmitting loop antenna is connected to the RF signal generator [IE909, International Electronics] via a RF power amplifier. Receiving loop

antennas (which are the duplicate of each other) are placed at a distance 1.75 m from the transmitting loop antenna. Reference transmitting antenna system is fed with different current levels at a certain frequency with the range of 8 kHz to 100 kHz. The corresponding signal

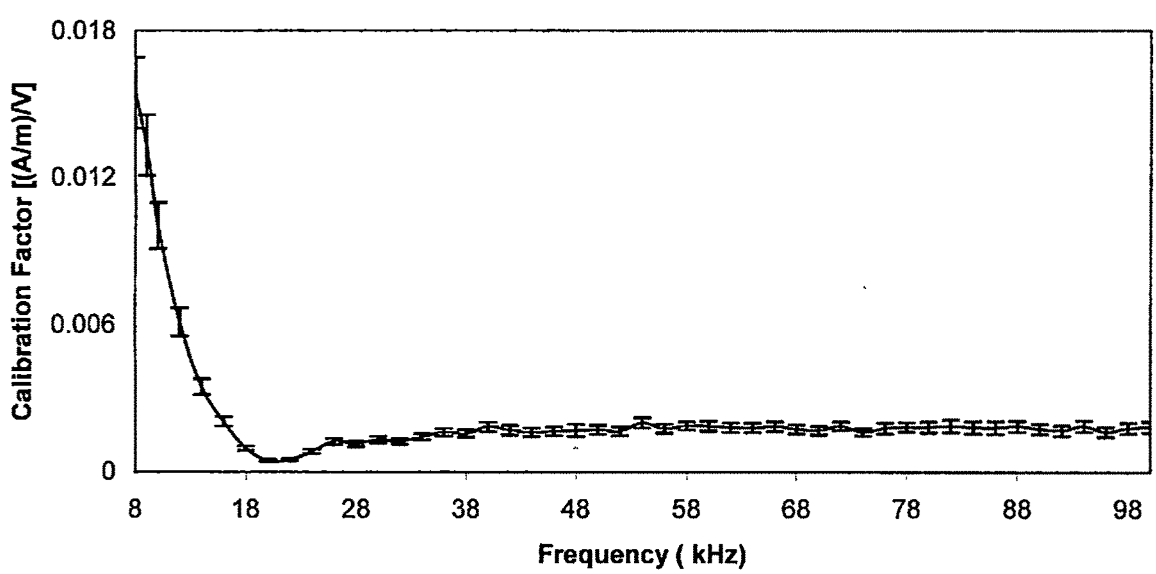

Figure 5.6 Calibration factor Vs frequency plot of the receiving loop antenna.

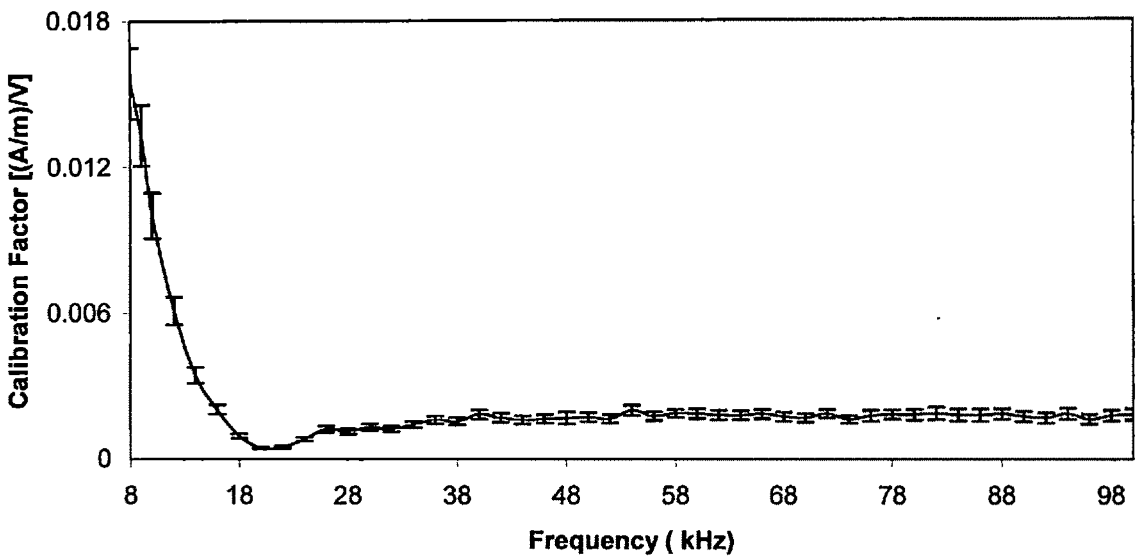

Figure 5.7 Calibration factor Vs frequency graph of the receiving loop channel 2

received by the receiving antenna is recorded by DSO and PC through GPIB interface. The expected field strength at the position of receiving antenna is calculated using equation 5.1.This value and the field strength actually recorded by the receiving antenna are used to find the calibration factor. Figure 5.6 shows the calibration factor Vs frequency of the radio receiving channel 1 and Figure 5.7 shows the calibration factor Vs frequency of the radio receiving channel 2.

5.2 The Preamplifier

The preamplifier is designed in such a ay that the useful signal is the current developed in the loop instead of voltage (due to the virtual ground of the op-amp) [Rudge82][Bruno01]. Op-27 operational amplifier is used because of its low intrinsic noise voltage (INV≈ 3nV/√HZ) compared with that of μA 741(INV-18nV/√HZ) or TL081 (90nV/√Hz). The input noise current being very low, it behaves as a low-impedance like loop and does not require a step-up transformer.

5.3- Band pass filter (BPF)

A +/- 40dB/decade band pass filter of pass band 8kHz – 80kHz is used in the front end electronics of each radio receiving channel.

5.4- Calibration of miniarray particle detectors

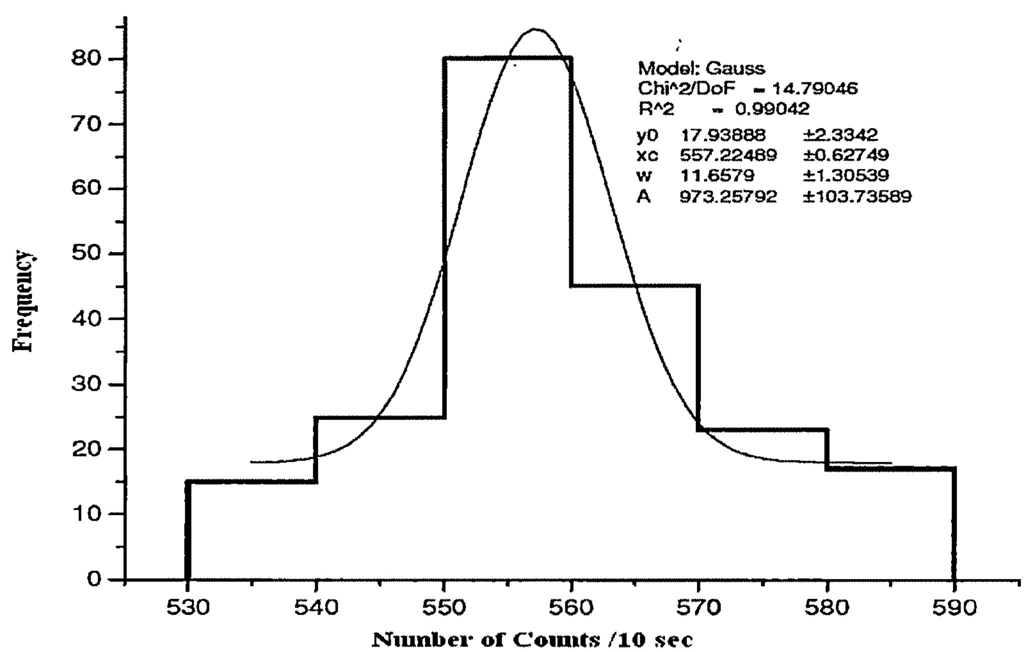

Figure 5.8 Statistical Fluctuation of Count Rate

The flux of the Hadron component and the soft component of secondary cosmic ray particles is $1.3 \times 10^2\, m^{-2}s^{-1}sr^{-1}$ and $0.5 \times 10^2\, m^{-2}s^{-1}sr^{-1}$. Thus the total flux of secondary cosmic ray particle in the sea level is $1.8 \times 10^2\, m^{-2}s^{-1}sr^{-1}$. The area of each scintillation block of miniarray particle detector is $0.25m^2$. Therefore the number of secondary cosmic ray particles crossing each miniarray particle detector per second is 45. The calibration of the detector for omni directional single particle pulse height is done by using a single channel analyzer ECIL, SC604B and a counter. The histograms for the distribution in the counts per 10 seconds are shown in Figure 5.8. The red line in the figure 5.8 shows the fitted Gaussian distribution with $\chi^2 = 14.79$.

5.5-Calibration of Discriminators

The individual channel of the discriminator boards is tested with the help of a commercial pulse generator and a counter. The test pulses from the pulse generator are fed to the input of the discriminator and the output is observed with the help of the counter.

5.6 Experimental setup for radio detection

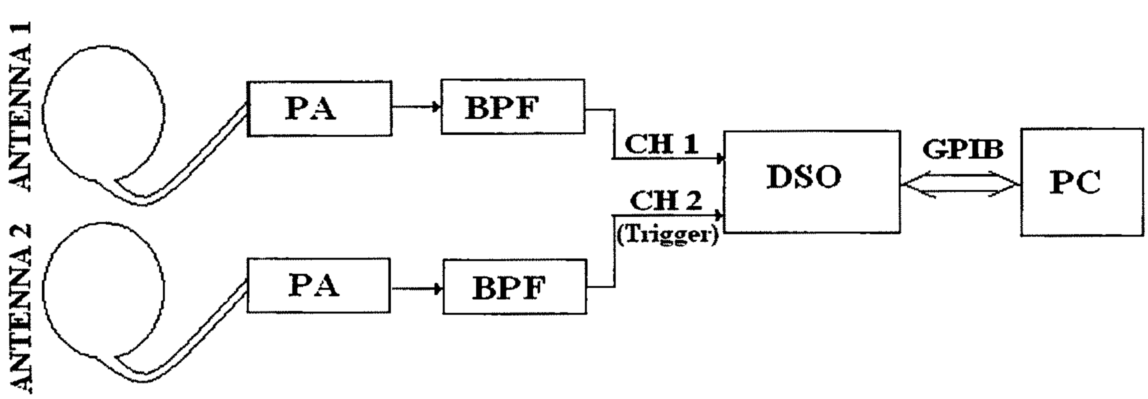

where- PA- Preamplifier, BPF-Band Pass Filter, DSO- Digital Storage Oscilloscope(TDS 520A,Tektronix, 500MHz, 500MS/s) PC- Personal Computer.

Figure 5.9 Block diagram of the experimental set up for radio detection alone.

The bias of the discriminator channel is adjusted to produce a definite count rate for the input test pulse. This setup run for a long time and does not show any appreciable change. The observed drift is also very negligible. The experimental setup in the miniarray research laboratory to detect radio signals alone is shown in the figure 5.9. Two loop antennas were installed in the rooftop of Physics building near the miniarray hut. Each antenna is placed at a distance of 2m from the miniarray hut. Signals from the antennas were processed by the VLF/LF front end electronics which consists of one low noise preamplifier and a band pass filter. Signals from the two radio channels are then fed to the Digital Oscilloscope TDS 520A, 500MHz. 500MS/s (Tektronix). The recorded signal is transferred to the PC via GPIB interface.

At first, the two radio channels were run simultaneously and data from both the channels were recorded .In this case the trigger signal for recording the radio data is derived from DSO's internal trigger, which is fixed at 130mV. PSD for the received signal from both the channels were calculated, which is discussed in Chapter VI.

In the next setup, the two radio channels are run simultaneously. However, instead of using DSO's internal trigger one radio channel is used to trigger the other. This ensures coincidence between the two radio channels and minimizes the reception of local radio noise. Electric field strength of the received signal by radio receiving channel 1 is calculated. The results are discussed in the Chapter VI.

5.7 Experimental setup for radio detection with miniarray

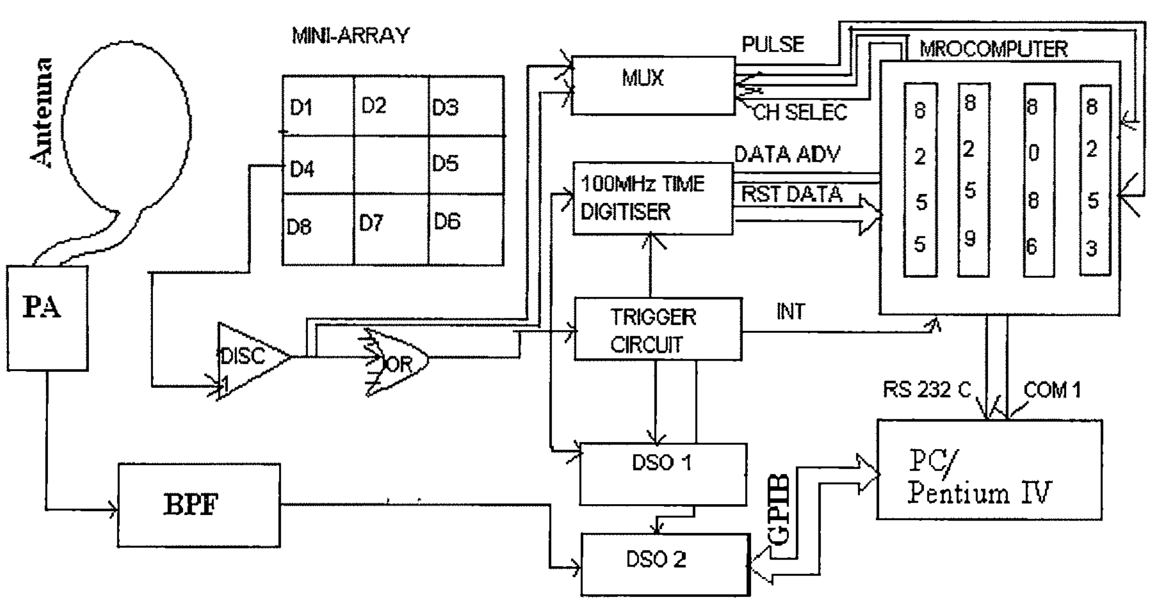

Figure 5.10 Block diagram of the experimental set up for radio signal detection in coincidence with miniarray.

References

[Bruno01] Marco Bruno, IK0ODO. Thinking about the ideal Loops. *http://www.vlf.it* (2001).

[Jean61] A G Jean, H E Taggart and J R Wait . *J.RES.NBS-C* **3**, 65 (1961).

[Rudge82] A.W.Rudge & A.d.Olver and P.Knight. *The Handbook of Antenna Design* (Peter Peregrinus Ltd.,London, 1982).

The miniarray particle detector setup is next used to trigger the radio detector, as shown in figure 5.10. The radio signal from the BPF is fed to one channel of DSO2 (TEKTRONIX TDS 520A) and the signal from (TEKTRONIX TDS 2022) are fed to the trigger channel of DSO2. This ensures that DSO2 records radio data whenever the miniarray detects a genuine cosmic ray event.

The experiment was run continuously for several days. However, no radio signal in coincidence with the UHE cosmic ray event was observed.

5.1.1 Design and Fabrication

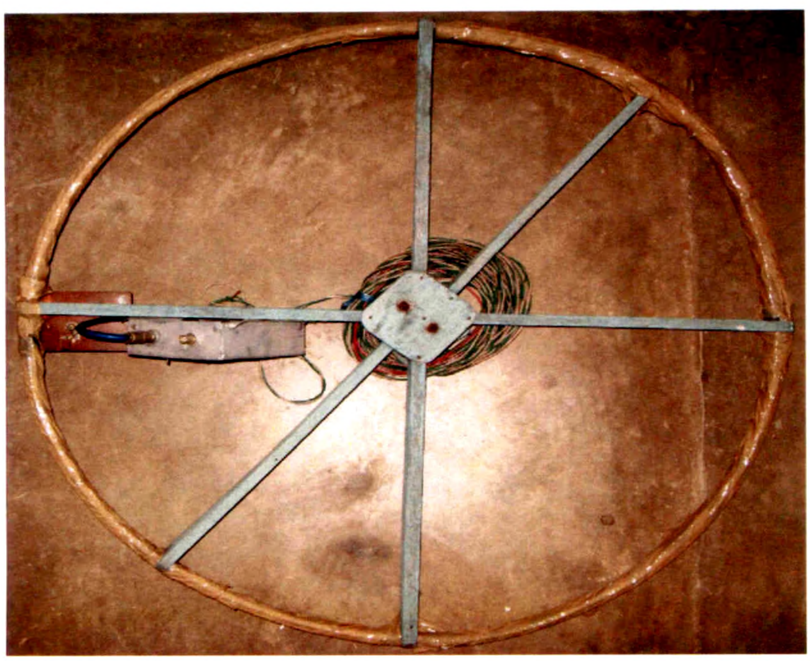

Figure: 5.2 Receiving antenna

Figure 5.2 shows the receiving loop antenna. Loop antenna frame is made of bamboo is of a circle of outer radius 37.5cm. The plain surface of 2" Casing- Capping pipe is affixed with adhesive in the outer surface of the rim. The rim is supported by a square frame made of wood to save it from any distortion of its shape and size. Enamel copper wire of AWG 21 is wound on the pipe, one turn at a time. The total number of turns is 40 and each turn is in contact with its nearest one. The upper part of the Casing capping pipe is now fixed and aluminum foil is wrapped around the whole loop with two small holes for connecting cables. Everything is covered with adhesive PVC tape to protect from weather. The aluminum shield is not indispensable; during all trials we have hardly found any difference between the antenna with shield and without it. Table 5.1 shows the antenna parameters.